AN APPROACH FOR THE AUTOMATIC DETECTION OF AGRICULTURAL FIELD SUB-BOUNDARIES FROM HIGH RESOLUTION SATELLITE IMAGES

YÜKSEK ÇÖZÜNÜRLÜKLÜ UYDU GÖRÜNTÜLERİNDEN TARIMSAL ARAZİ ALT-SINIRLARIN OTOMATİK TESPİTİ İÇİN BİR YAKLAŞIM

SAMAN GHAFFARIAN

PROF. DR. MUSTAFA TÜRKER

Supervisor

Submitted to Institute of Sciences of Hacettepe University as a

Partial Fulfillment of the Requirements

for the Award of the Degree of Master

in Geomatics Engineering

December 2014

This work named **"AN APPROACH FOR THE AUTOMATIC DETECTION OF AGRICULTURAL FIELD SUB-BOUNDARIES FROM HIGH RESOLUTION SATELLITE IMAGES"** by **SAMAN GHAFFARIAN** has been approved as a thesis for the Degree of **MASTER OF SCIENCE IN GEOMATICS ENGINEERING** by the below mentioned Examining Committee Members.

Prof. Dr. Erhan TERCAN
Head .....

Prof. Dr. Mustafa TÜRKER
Supervisor .....

Asst. Prof. Dr. Metin NOHUTCU
Member .....

Asst. Prof. Dr. Yakup ÖZKAZANÇ
Member .....

Asst. Prof. Dr. Emre SÜMER
Member ..... 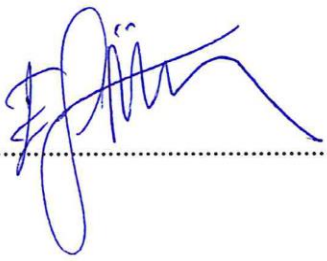

This thesis has been approved as a thesis for the Degree of **MASTER OF SCIENCE IN GEOMATICS ENGINEERING** by Board of Directors of the institute for Graduate Studies in Science and Engineering.

Prof. Dr. Fatma SEVİN DÜZ
Director of the Institute of
Graduate School of Science and Engineering

To My Parents

ETHICS

In this thesis study, prepared in accordance with the spelling rules of Institute of Graduate Studies in Science of Hacettepe University,

I declare that

- all the information and documents have been obtained in the base of the academic rules,
- all audio-visual and written information and results have been presented according to the rules of scientific ethics,
- in case of using other Works, related studies have been cited in accordance with the scientific standards,
- all cited studies have been fully referenced,
- I did not do any distortion in the data set,
- and any part of this thesis has not been presented as another thesis study at this or any other university.

16/01/2015

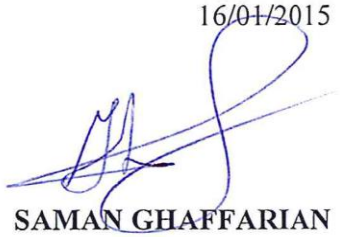

SAMAN GHAFFARIAN

ABSTRACT

AN APPROACH FOR THE AUTOMATIC DETECTION OF AGRICULTURAL FIELD SUB-BOUNDARIES FROM HIGH RESOLUTION SATELLITE IMAGES

Saman Ghaffarian

Master of Science, Department of Geomatics Engineering

Supervisor: Prof. Dr. Mustafa TÜRKER

December 2014, 82 pages

Agricultural crop mapping is quite important for crop yield estimation in regional and national scale. Remote sensing images are popular data to identify and classify land cover types in the agricultural areas. The recent image classification techniques for agricultural areas use approaches which work on field-by-field basis by means of assigning a crop label for each agricultural field individually. In field-based classification approaches, the classification is performed within the permanent agricultural field boundaries that are stored in a geographical information system (GIS) as vector polygons. However, crop variation within the fields is an important problem to be solved. To solve this problem, image segmentation is needed to be executed to extract the sub-boundaries within the

permanent boundaries of the fields and subsequently to achieve higher accuracy in field-based classification operations.

In this study, a field-based segmentation approach is proposed to extract within-field sub-boundaries from high resolution remotely sensed images. The within-field sub-boundary extraction operation is carried out one field at a time by means of processing each field separately. First, the within-field edges are detected using the Canny edge detection algorithm and the image is clustered using an automatic Fuzzy C-means (FCM) clustering algorithm. To automate the FCM clustering algorithm, the algorithm is executed iteratively starting with the assumption that the fields contain maximum six sub-fields that correspond to six clusters. After the first iteration, the Euclidean distances between the cluster centers are computed. If at least one distance stays below a defined threshold value, the number of sub-fields is decreased by one and the clustering operation is repeated with the reduced number of clusters. This iterative execution of the FCM clustering algorithm is carried out until all the distances between the cluster centers stay above the threshold value. Next, the external forces for the Gradient Vector Flow (GVF) Snake are calculated based on the detected edges and the clusters. To calculate and construct the gradient vectors, the distances between the pixels are computed within each cluster so as to steer the contours toward the correct boundaries. After computing the external forces, a novel cluster-based method is used to seed the GVF Snake by means of constructing an ellipse for each cluster that fall within the field. After that, the GVF Snake is executed for detecting the within-field sub-boundaries. As the final step, the detected sub-boundaries are simplified through a line simplification algorithm and thus the final appropriate sub-boundaries are extracted.

The developed approach was implemented in an agricultural area in Karacabey, Bursa plain located in north-west of Turkey. The high resolution satellite images used include the Ikonos multispectral (XS) image acquired in 15 July 2004 and the Quickbird multispectral (XS) and pansharpened (PS) images acquired in 13 August 2004.The results achieved are quite promising. The overall sub-boundary extraction accuracies through the proposed automatic approach were computed to be 93.61%, 84.96% and 88.78% for the Ikonos (XS), Quickbird (XS) and Quickbird (PS) images, respectively.

Keywords: Boundary Detection, Field-Based, GVF Snake, Image Segmentation, Agriculture, FCM Clustering.

ÖZET

YÜKSEK ÇÖZÜNÜRLÜKLÜ UYDU GÖRÜNTÜLERİNDEN TARIMSAL ARAZİ ALT-SINIRLARIN OTOMATİK TESPİTİ İÇİN BİR YAKLAŞIM

Saman Ghaffarian

Yüksek Lisans, Geomatik Mühendisliği Bölümü

Tez Danışmanı: Prof. Dr. Mustafa TÜRKER

Aralık 2014, 82 Sayfa

Tarımsal ürün haritalama, bölgesel ve ulusal ölçekte mahsul verim tahmini için oldukça önemlidir. Uzaktan algılama görüntüleri tarım alanlarında arazi örtüsü türlerini belirlemek ve sınıflandırmak için popüler verilerdiler. Tarım alanları için son görüntü sınıflandırma teknikleri, her tarım parseli için bir sınıf etiketi atama yoluyla parsel bazlı yaklaşımları içerirler. Parsel bazlı sınıflandırma yaklaşımında, sınıflandırma bir coğrafi bilgi sisteminde (CBS) depolanan tarım parsellerinin kalıcı sınırları içinde gerçekleştirilir. Ancak, parsellerin içinde ürün değişimi çözülmesi gereken önemli bir sorundur. Bu sorunu çözmek için, görüntü bölütleme alanları daimi sınırları içinde kalan alt sınırları çıkarmak için gereklidir. Elde edilen alt sınırlar parsel bazlı sınıflandırma işlemlerinde yüksek sınıflandırma doğruluğu elde etmek için gereklidir.

Bu çalışmada, tarımsal parseller içindeki alt sınırları yüksek konumsal çözünürlüklü uydu görüntülerinden çıkarmak için bir parsel-tabanlı bölütleme yaklaşımı önerilmektedir. Parsel içi alt sınır çıkarma işlemi her parsel ayrı işlenmek suretiyle, parsel parsel gerçekleştirilir. Başlangıçta, alt parsellerin kenarları Canny Edge Detection algoritması kullanılarak tespit edilir ve görüntü bir otomatik Fuzzy C-Means (FCM) kümeleme algoritması ile kümelenir. FCM kümeleme işlemini otomatikleştirmek için, algoritma iteratif bir şekilde, her parselin maximum altı alt-parsel içerdiği varsayımı ile ki altı kümeye karşılık gelir, uygulanır. Ilk iterasyondan sonra, küme merkezleri arasındaki Öklid mesafeleri hesaplanır. En az bir mesafe belirli bir eşik değerinin altında kalırsa, alt-alanların sayısı bir azaltılır ve kümelenme işlemi azaltılmış küme sayısı ile tekrarlanır. FCM kümeleme algoritmasının bu iteratif işlemi küme merkezleri arasındaki tüm mesafeler eşik değerinin üzerinde kalinciya kadar gerçekleştirilir. Sonra belirlenen kenarlara ve kümelere göre Gradient Vector Flow (GVF) Snake için dış güçler hesaplanır. Doğru sınırlarına doğru konturları yönlendirmek amacıyla, gradient vektörleri hesaplamak ve inşa etmek için, her küme içinde pikseller arasındaki mesafeler hesaplanır. Dış güçleri hesapladıktan sonra, parsel için düşen her küme için bir elips inşa ederek GVF Snake başlatmak için yeni bir küme-tabanlı yöntem kullanılır. Bundan sonra, parsel içi alt sınırları tespit etmek için GVF Snake çalıştırılır. Son adım olarak, tespit edilen alt sınırlar bir çizgi basitleştirme algoritması ile basitleştirilir ve böylece nihai uygun alt-sınırlar tespit edilir.

Geliştirilen yaklaşım, Türkiye'nin kuzey-batısında bulunan Bursa ili, Karacabey ilçesinde bir tarım alanı üzerinde uygulanmıştır. Kullanılan yüksek çözünürlüklü uydu görüntüleri Quickbird çok bantlı (XS) ve keskinleştirilmiş (PS) görüntüler ve 15 Temmuz 2004 tarihli 13 Ağustos 2004 tarihli İkonos çok bantlı (XS) görüntüsüdür. Elde edilen test sonuçları oldukça umut vericidir. Önerilen yaklaşım ile, otomatik olarak çıkartılan alt sınırların genel doğrulukları, Ikonos (XS), Quickbird (XS) ve Quickbird (PS) görüntüler için sırasıyla 93.61%, 84.96%, ve 88.78% olarak hesaplanmıştır.

Anahtar Kelimeler: Sınır Tespiti, Alan Bazlı, GVF Snake, Görüntü Bölütleme, Tarım, FCM Kümeleme.

ACKNOWLEDGEMENTS

Foremost, I would like to express my sincere gratitude to my advisor PROF. DR. Mustafa TÜRKER for the continuous support of my MSc study and research, for his patience, motivation, enthusiasm, and immense knowledge.

This thesis is dedicated to my parents who have given me the opportunity of an education from the best institutions and support throughout my life.

TABLE OF CONTENTS

Page

ABSTRACT ..... *i*

ÖZET ..... *iii*

ACKNOWLEDGEMENTS ..... *v*

TABLE OF CONTENTS ..... *vi*

LIST OF TABLES ..... *viii*

LIST OF FIGURES ..... *ix*

SYMBOLS AND ABBREVIATIONS ..... *x*

1.Introduction *1*

1.1. Objectives **3**

1.2. Contributions **3**

1.3. Thesis Outline **4**

1.4. Software **4**

2. *The Literature Review* **5**

2.1. Field-based Image Segmentation Methods **5**

2.2. Field-based Image Segmentation Based on the Snake Algorithm **6**

3. Methodology ***8***

3.1. Computation of the NDVI Image **10**

3.2. Detection of the Edges **10**

3.3. Within Field Clustering **12**

3.3.1. Fuzzy C-means Clustering Based on Special Rules **12**

3.3.2. Refinement of the Clusters **14**

3.4. Primary Contour Detection using the Improved Gradient Vector Felow (GVF) Snake Algorithm **15**

3.4.1. Calculating the External and Internal Forces **16**

3.4.2. Automatic Initialization **19**

3.4.3. The Execution of the Improved GVF Snake Algorithm **21**

3.4.4. Bounday Masking **22**

3.5. Line Simplification **23**

3.6. Forming the Sub-Polygons Within the Fields Using a Recursive Algorithm **24**

3.7. The Evaluation Methodology **26**

4. Results and Analysis ***31***

4.1. Study Area **31**
4.2 Data Sets **32**
4.2.1 Raster Data **32**
4.2.2 Vector Data **32**
4.3. Results and Discussion **33**
4.3.1 The Results of the Ikonos Multispectral Image **39**
4.3.2 The Results of the QuickBird Multispectral Image **44**
4.3.3 The Results of the QuickBird Pansharpened Image **50**
5. Conclusions and Recommendations ***56***
5.1. Conslusions **56**
5.2. Recommendations **57**
REFERENCES ***59***
APPENDIX ***64***
CURRICULUM VITAE ***67***

LIST OF TABLES

Page

Table 1 The spatial and spectral properties of the Ikonos and the QuickBird satellite images 32
Table 2 The area and number of sub-fields for the test fields 34
Table 3 The parameters and the threshold values used for the Ikonos, QuickBird XS, and QuickBird PS images 35
Table 4 The overall accuracies for the Ikonos, QuickBird XS and QuickBird PS images 36
Table 5 The segmentation grouping of the results obtained for the Ikonos, QuickBird XS, and QuickBird PS images 37
Table 6 The accuracy grouping of the results obtained for the Ikonos, QuickBird XS, and QuickBird PS images 38
Table 7 For the Ikonos image, the computed NDVI image, the extracted edges, the clustering results, the permanent field boundaries (red), the extracted sub-field boundaries (blue), and the accuracies of the test fields. (1-Tomato, 2-Corn, 3-Residue, 4-Onion, 5-Sugar Beet, 6-Orchard, 7-Pepper, 8-Rice, 9-Clover, 10-Plowed) 41
Table 8 For the QuickBird XS image, the computed NDVI image, the extracted edges, the clustering results, the permanent field boundaries (red), the extracted sub-field boundaries (blue), and the accuracies of the test fields. (1-Tomato, 2-Corn, 3-Residue, 4-Onion, 5-Sugar Beet, 6-Orchard, 7-Pepper, 8-Rice, 9-Clover) 47
Table 9 For the QuickBird PS image, the computed NDVI image, the extracted edges, the clustering results, the permanent field boundaries (red), the extracted sub-field boundaries (blue), and the accuracies of the test fields. (1-Tomato, 2-Corn, 3-Residue, 4-Onion, 5-Sugar Beet, 6-Orchard, 7-Pepper, 8-Rice, 9-Clover) 53

LIST OF FIGURES

Page

Figure 3.1 The proposed image segmentation method 9
Figure 3.2 For the selected four fields (#1, #3, #7, and #13 test images) the results of the Edge Detection Operation as applied to Ikonos satellite image 12
Figure 3.3 For the selected two sample fields, the results of clustering the QuickBird PS satellite image 15
Figure 3.4 (a) A cluster of the field #13 obtained through clustering the Ikonos image and the corresponding ellipse (seed contour), (b) the features of the corresponding ellipse 20
Figure 3.5 The illustration of the initialization procedure for the seeding operation for field #13 using the Quickbird PS image 21
Figure 3.6 The illustration of the improved GVF snake steps for field #13 using the Quickbird PS image 22
Figure 3.7 For the selected four fields; (a) the Quickbird PS image and (b) the sub-boundaries (blue) after the line simplification operation 24
Figure 3.8 The hash table for the connected segments in a sample field 25
Figure 3.9 All cycle paths for node A 26
Figure 3.10 For a simple field, the comparison of the geometries between the truth sub-fields (T1, T2, T3, T4) and the extracted result sub-fields (R1, R2, R3) [33] 29
Figure 4.1 The location of the study area in Turkey 31

SYMBOLS AND ABBREVIATIONS

GIS	Geographical Information Systems
GVF	Gradient Vector Flow
FCM	Fuzzy C-Means
IRS	Indian Remote Sensing Satellite
LISS	Linear Imaging Self-Scanning Sensor
NDVI	Normalized Difference Vegetation Index
NIR	Near Infra Red
UTM	Universal Transverse Mercator
PS	Pan Sharpened
OBIA	Object-Based Image Analysis

1. Introduction

Agriculture is one of the most important factors in the economies of developed and undeveloped countries alike. Indeed, production of food and the cost of producing food are the key points for the politics of every country. Moreover, due to the rapid increase of urban population, the need for food is significantly increasing in Turkey along with all other countries. Thus, the demand of agricultural products has gained more importance to provide agricultural needs. In order to make decisions for the future many analyses are needed to be conducted to observe and control the agricultural status of the fields. These decisions are important for both farmers individually and the governmental foundations.

The mapping and identification of the crop fields supply extensive knowledge about the agricultural products. These knowledge serve purpose of yield estimation, crop rotation records, finding the factors that influence the crop stress, collecting crop production statistics, mapping soil productivity, evaluating the crop damage due to disasters such as drought and storms, and monitoring the farming activities. Traditionally, up-to-date information is generally acquired by farmer declarations and/or ground visits of the fields. However, these methods are inefficient in terms of time and cost aspects and may contain inaccurate results due to utilizing non-standard measurements. Therefore, robust and reliable automated methods are required for the rapid and accurate identification of the crop types of agricultural lands. In the last decade, the availability of high spatial resolution satellite images have increased due to the improvements in satellite sensor technologies. Furthermore, due to improvements in digital image processing and analysis techniques, remote sensing images can be used as an efficient and reliable solution for the mapping and identification of the crop types.

Automatic image classification is the most frequently used image processing technique for detecting crop fields from remote sensing images. There are two main image classification techniques; pixel-based and field-based (also named object-based or polygon-based) classification methods. Pixel-based classification methods try to label each pixel individually, considering the pixel as the main element. However, this method may cause various errors in image classification procedures. To overcome these limitations, field-based classification methods are used. The field-based classification methods take group of pixels (segments) as the main element and try to label the fields and therefore all the pixels that fall within the fields. These methods provide considerably accurate results in

comparison with the pixel-based methods [13], [17], [18], and [19]. In order to group (segment) the pixels of an image into homogenous groups a pre-processing technique called image segmentation is performed [17], [26]. Image segmentation is a process of determining homogenous areas in the image. Analyzing the groups of pixels within the segments based on their textural and contextual properties are necessary to extract more meaningful objects, which is the major interest of Geographic Object-Based Image Analysis (GOBIA) community [47], [48]. In most of the GOBIA literatures, researchers try to develop efficient segmentation methods in order to utilize in GOBIA, which demonstrate the importance of the use of image segmentation in these issues [29], [30], and [49].

Several image segmentation methods have been developed in order to segment the remotely sensed images [25], [27]. The three primary methods which are utilized in image segmentation are the edge-based methods, the region-based methods, and the hybrid methods. In edge-based methods, the detected edges in an image are assumed to represent object boundaries, and they are used to identify these objects [50]. An edge-based technique may attempt to find the object boundaries and then locate the object itself by filling them in. In region-based methods, the region-based segmentation algorithms operate iteratively by grouping together the pixels which are neighbors and have similar values and splitting the groups of pixels which are dissimilar in value [51]. The hybrid methods use the combination of the edge and region data [30], [32], and [33].

Generally, each method has advantages and disadvantages, and each one may be efficient in some special fields. Moreover, an important problem for segmenting the whole image is that it contains various objects in addition to agricultural fields. Indeed, in this case image segmentation method should deal with the other objects such as roads, ditches, hedges and streams which should not belong to any of the crop field segments. Therefore, a prior knowledge about the permanent agricultural field boundaries becomes significant in order to remove or reduce the effects of the other objects in the image. The prior knowledge can be stored and available in a Geographical Information Systems (GIS). The use of permanent field boundary data stored in a GIS in image segmentation demonstrates the important point for extracting sub-boundaries within the crop fields.

Therefore, in this thesis, an approach is presented for the automatic extraction of dynamic crop boundaries within the permanent agricultural field boundaries stored in a GIS

database. The tests of the approach was carried out in an agricultural area located near Karacabey, Bursa in north-west of Turkey using the Ikonos multispectral (XS) image acquired in 15 July 2004 and the Quickbird multispectral (XS) and pansharpened (PS) images acquired in 13 August 2004.

1.1. Objectives

The main objectives of this thesis are:

- to develop an automatic field-based image segmentation approach for extracting the sub-boundaries within the permanent agriculture field boundaries,
- to assess the suitability of an improved Gradient Vector Flow (GVF) Snake to delineate the agricultural sub-field boundaries,
- to analyze the pros and cons of the proposed method on the obtained results, and
- to provide a robust and reliable input dataset for the field-based classification methods to help improve the accuracies which may become low due to within field crop variations.

1.2. Contributions

The first and major contribution of this thesis is developing a Snake-based method to extract agricultural sub-field boundaries. The second contribution of the thesis is developing a method to automate the FCM clustering algorithm to cluster agricultural fields. The calculation of the gradients in the clustered image based on the computed cluster distances is the third contribution. The fourth contribution of the study is the development of a novel automatic GVF Snake algorithm based on the output of the FCM clustering algorithm. The improvement of the GVF Snake algorithm by supplying a novel cluster-based external force along with the commonly used external forces is the fifth contribution. The final contribution of the thesis is the development of a method based on simple rules and Douglas-Peucker algorithm for the post-processing of the improved GVF Snake outputs to obtain accurate segmentation results.

1.3. Thesis Outline

The remaining part of the thesis is organized in four sections. Section 2 demonstrates an overall review of the methods used for performing the field-based image segmentation and the Snake (Active contours) algorithms. Section 3 states the proposed methodology named "An Approach for the Automatic Detection of Agricultural Sub-Field Boundaries from High Resolution Satellite Images". In section 4, the study area and the data sets are described as well as presenting the results and critical discussions of the execution of the proposed method on test data. Finally, in section 5, the conclusions and recommendations for the future research are given.

1.4. Software

The proposed automatic Snake-based image segmentation method was implemented through a program written in the MATLAB programming environment (Appendix A).

2. The Literature Review

Image segmentation is a well-known problem in image processing and computer vision. It is mainly the process of determining the homogeneous areas in an image. Furthermore, image segmentation can be utilized as a pre-process to extract these homogeneous regions to be classified by a classification operation, particularly through object-based classification methods. Furthermore, it is frequently used for extracting agricultural field boundaries that contain important knowledge to be used in a number of applications that include

- object-based classification of the agricultural fields,
- derivation of the potential wind erosion risk fields for geo-scientific queries, which can be generated with additional information about the dominant wind direction, wind shelters, soil roughness, soil moisture etc. [1], and
- precision farming to the monitoring of subsides [2], [3] and [4].

2.1. Field-based Image Segmentation Methods

Field-based agricultural statistics such as mean, mode, variance and so on are valuable information to determine the boundaries of agricultural fields which can be utilized in many applications, such as the within-field crop yield forecasting [5], quantifying the parcel-level water-use [6], and including the crop temporal relationships in the classification operation [7].

Field-based image segmentation methods are also known as object- and polygon-based image segmentation methods. A significant number of studies exist regarding object-based (field-based) classification methods and the comparative analyses among these methods and the pixel-based methods. Per-pixel classification methods classify the image and extract the statistical characteristics of the objects (fields in this case) on the basis of thematic per-pixel classification algorithms and the final class assignment of a field is usually carried out regarding the individual pixels falling within the field [8]-[19]. On the other hand, field-based classification methods generally use image spectral band information, such as the Normalized Difference Vegetation Index (NDVI) or the other

relations between the spectral bands to extract the statistical characteristics of the objects (fields) [20]-[27].

Janssen and Molenaar [26] proposed an object based strategy which includes three steps using the Landsat TM image to update field boundaries and the crop types of the agricultural fields alike. They utilized information about the dynamics of object geometry to extract field boundaries. They reported good agreement between the resulting field geometry and the field geometry extracted by a photo-interpreter among integration of remote sensing in a Geographical Information Systems (GIS) application. Ji [28] used the dyadic wavelet transform to extract field boundaries directly form a Landsat TM imagery. Although the majority of the field boundaries were delineated, they discussed that the use of a single image is not adequate to delineate some of the fallow field boundaries as well as boundaries among the cropped fields with the similar spectral characteristics. Rydberg and Borgefors [29] used multispectral satellite images for the automatic extraction of agricultural field boundaries. They integrated the multispectral edge information from a gradient-based edge detector with the segmentation obtained using a simple ISODATA clustering algorithm. In addition, their results were shown to be quite promising with 87% accuracy. Mueller et al. [30] proposed an object-based segmentation method with special focus on shape analysis to extract large, man-made objects, particularly agricultural fields from high resolution panchromatic satellite images. The main idea of their proposed method is based on the integration of region- and edge-based techniques. They discussed the lack of possibilities to control the segmentation process using the straight region boundaries of low contrast districts. Ishida et al. [31] used multi-resolution wavelet transform to detect the edges of submerged paddy fields from SPOT image. Their results were satisfactory in practice. In a recent study carried out by Turker and Kok [32], [33] a model was developed to automatically extract dynamic sub-boundaries within the existing agricultural fields from remote sensing imagery. The overall accuracy performances were computed to be 82.6% and 76.2% for the SPOT5 and SPOT4 images, respectively.

2.2. Field-based Image Segmentation Based on the Snake Algorithm

Snake, which was first introduced by Kass et al. [34], is a widely used algorithm to delineate objects precisely. Snake is a sophisticated image processing technique that

combines image features with the shape constraints in an energy minimization process. In the past, several studies have been carried out regarding the delineation of the agricultural field boundaries using the Snake algorithm. Torre and Radeva [35] integrated region growing and Snakes for the segmentation of agricultural fields. The technique was called a region competition technique. Since they make the initialization manually, their method of segmentation can be considered semi-automatic and therefore, it is time-consuming. Butenuth et al. [36] presented a field-based segmentation method based on the watershed segmentation and the snake algorithms. The method starts with the watershed segmentation and the subsequent grouping of the resulting basins. The potential field areas are divided, if necessary, into smaller and more detailed fields using a line extraction technique or by using a prior GIS vector data. Subsequently, the results are used to initialize the snake algorithm in order to get the final segmentation output. Tiwari et al. [37] developed an automatic approach for the extraction of field boundaries from the IRS P-6 LISS IV dataset. Their segmentation method uses the tonal and textural gradients to derive preliminary field boundaries. The derived field boundaries are geometrically refined using the snake algorithm. However, several problems (gaps, overlaps) were reported in the final results. Butenuth and Heipke [38] presented Network Snake as a graph-based object delineation approach with the active contour models. They integrated the graph-based method, which is an optimization method, with the snake algorithm. They tested the method on a pansharpened Ikonos image covering an agricultural area for delineating the field boundaries. To initialize the network snake, they utilized an edge-based region growing method. However, the results of the Network snake algorithm showed several problems. The network snake highly depends on the initial contours, and it cannot change the topology characteristics of the active contours. This is due to the structure of the network snake and its conjunction properties, which was initially entered. Consequently, if the topology properties of the seeding points include incorrect information, they cannot be corrected during the evolution of the active contours and this would lead to inaccurate results.

3. Methodology

This section describes the method and the flow of the thesis study conducted. The flowchart of the methodology (Figure 3.1) shows the processes of the improved GVF snake algorithm for extracting the sub-boundaries within the agricultural fields.

The input data consist of a high resolution image covering an agricultural area and the permanent field boundaries that are stored in a Geographic Information Systems (GIS) as vector polygons. After the pre-processing of the data, the edge detection and clustering operations are carried out in parallel. In order to detect the edges, the Canny edge detector is performed on the NDVI image of each field on field-by-field basis. In parallel with the edge detection operation, an automated FCM clustering is carried out on the image covering the field. Then, the external forces, which will be used in the improved GVF snake algorithm, are computed based on the edge image and the clustered image. Next, the improved GVF snake algorithm is seeded using the clustered image by considering each cluster as a sub-field within the permanent field. To automatically execute the improved GVF snake algorithm for extracting the preliminary sub-boundaries both the external forces and the initial contours are used. To use in the boundary-masking step, a buffer zone is generated around the permanent field boundaries. In the boundary masking step, the primary contours that fall within the buffer zone are removed. Next, several line simplification techniques are applied in order to obtain appropriate straight sub-boundaries. Finally, sub-fields (sub-polygons) are constructed using a recursive method that utilizes the connections of the line segments.

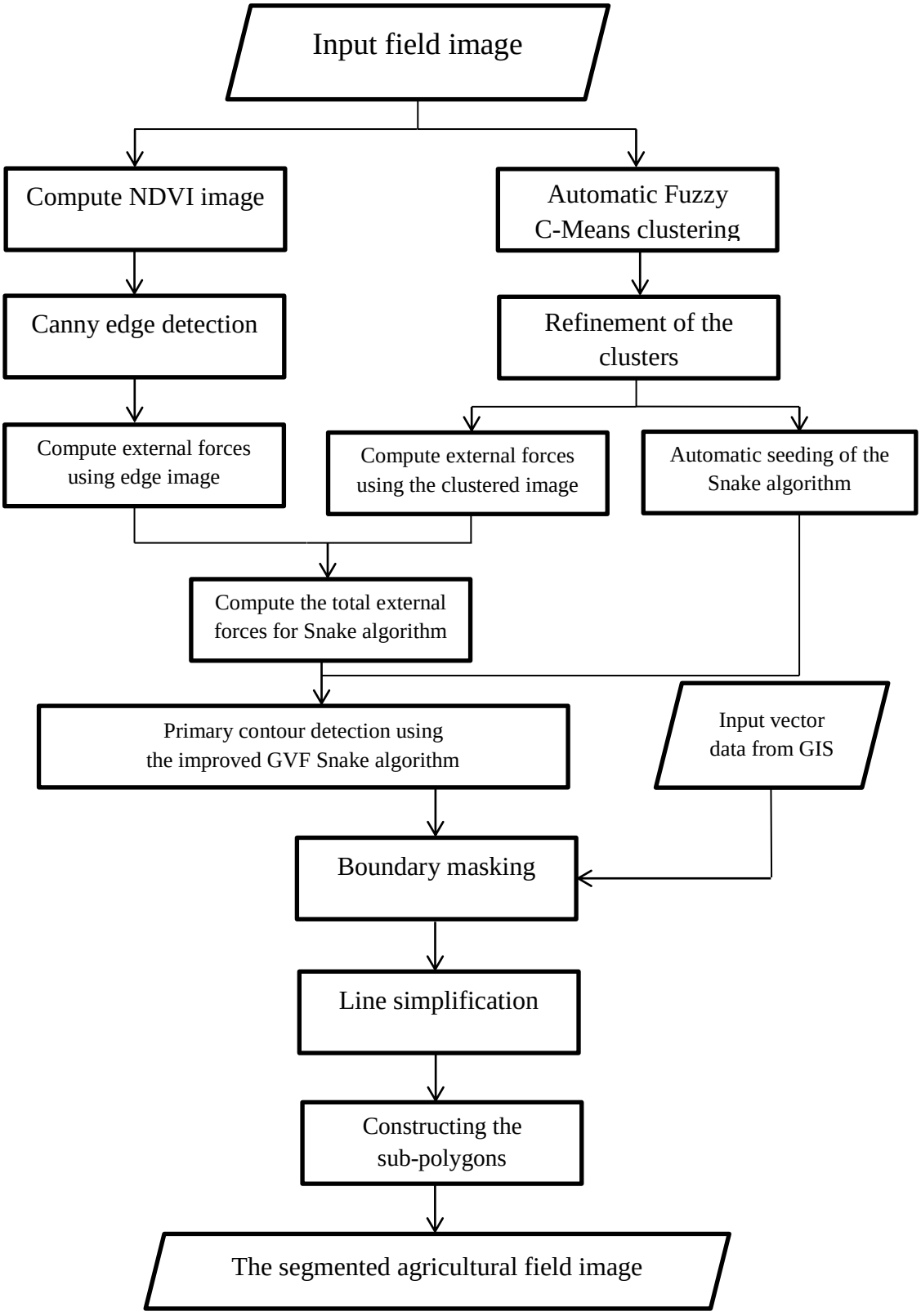

Figure 3.1. The proposed image segmentation method.

3.1. Computation of the NDVI image

To determine the density of green on a patch of land, researchers must observe the distinct colors (wavelengths) of visible and near-infrared sunlight reflected by the plants. When sunlight strikes objects, certain wavelengths of this spectrum are absorbed and other wavelengths are reflected. The pigment in plant leaves, chlorophyll, strongly absorbs visible light (from 0.4 to 0.7 μm) for use in photosynthesis. The cell structure of the leaves, on the other hand, strongly reflects near-infrared light (from 0.7 to 1.1 μm). The more leaves a plant has the more these wavelengths of light are affected. Nearly all satellite Vegetation Indices employ the difference formula below (Equation 3.1) to quantify the density of plant growth [47]. The result of this formula is called the Normalized Difference Vegetation Index (NDVI). Calculation of the Normalized Difference Vegetation Index (NDVI) based on the brightness values, is as follows:

$$NDVI = \frac{NIR - RED}{NIR + RED} \tag{3.1}$$

where RED and NIR stand for the spectral reflectance measurements acquired from the red and near-infrared bands of the image, respectively.

3.2. Detection of the Edges

Edge detection is one of the fundamental operations in image processing with the numerous approaches to it. Edge detection refers to the process of identifying and locating sharp abrupt changes in pixel intensity in an image, characterizing boundaries of objects in a scene. The Canny Edge Detection method [39] is generally known as a superior edge detection compared to other edge detection methods and is widely used in computer vision. Thus, in this study the Canny edge detector was selected to be used for detecting the edges throughout the proposed approach.

The popularity of the Canny edge detector can be attributed to its optimality according to three criteria of good detection, good localization, and single response to an edge [40]. It also has a rather simple approximate implementation. A typical implementation of the Canny edge detector follows the following steps.

1. Smooth the image with an appropriate Gaussian filter to reduce desired image details.
2. Determine gradient magnitude and gradient directions at each pixel.
3. If the gradient magnitude at a pixel is larger than those at its two neighbors in the gradient direction, then mark the pixel as an edge. Otherwise, mark the pixel as the background (non-edge).
4. Remove the weak edges by hysteresis thresholding.

Hysteresis uses two threshold values that are the low and high thresholds. If the magnitude of a pixel is below the low threshold value, it is decided as the non-edge. If the magnitude of a pixel is above the high threshold value, then it is decided as the non-edge except if the pixel under consideration has a connection to a pixel with a gradient below the high threshold.

Indeed, the low and high thresholds are used in order to reduce or increase the amount of the edges. Therefore, relying on purpose of using the Canny edge detector these thresholds can change. Furthermore, various thresholds can be selected considering image types, such as image resolution, which the Canny edge detection method is going to be executed on them.

In the proposed segmentation method, the Canny edge detector is applied on the derived NDVI image. Three-combinations of the low and high threshold values were set considering the diversity of the fields and the resolution of the images used. In this study, the low and high threshold values were selected based on a trial and error technique.

The result of the Canny edge detector is a binary image which consists of black pixels that illustrate the edge lines and the white pixels that represent the non-edge pixels. For the selected several fields, the results of the edge detection operation performed on the Ikonos satellite image are illustrated in Figure 3.2.

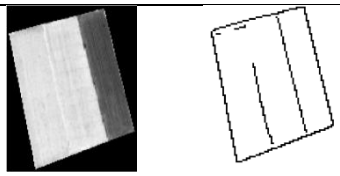	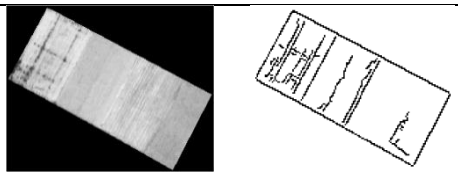
a) Test field #1 and the output edge detection	b) Test field #3 and the output of edge detection
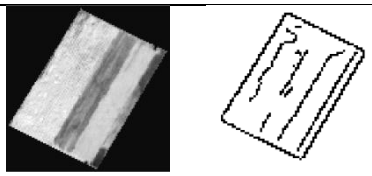	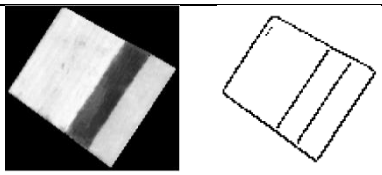
c) Test field #7 and the output of edge detection	d) Test field #13 and the output of edge detection

Figure 3.2. For the selected four fields (#1, #3, #7, and #13 test fields) the results of the Edge Detection Operation as applied to Ikonos XS satellite image.

3.3. Within Field Clustering

3.3.1. Fuzzy C-means (FCM) Clustering Based on Special Rules

A fuzzy set is a class of objects that has a continuum of grades of membership. Such a set is characterized by a membership (characteristic) function that assigns a grade of membership that ranges from zero to one for each object [41], [42]. The FCM clustering is an iterative clustering method that produces optimal c-partitions by minimizing the weighted dissimilarity function [43].

Let X_{ib} $(i = 1,2,..., N)$ represents a B-dimensional vector (where B is the number of bands in an image), and N is the number of data points (N = Number of image pixels); this notation is used to determine the cluster centers CC_{kb} for the k^{th} cluster and its b^{th} dimension by using the expression given below:

$$CC_{kb} = \frac{\sum_{i=1}^{N} U_{ikb}^{f} X_{ib}}{\sum_{i=1}^{N} U_{ikb}^{f}} \tag{3.2}$$

where

U is the membership matrix, which has the size N × C × B and is first initialized randomly such that $U_{ikb} \in [0,1]$ and $\sum_{k=1}^{C} U_{ikb} = 1.0$, for each i and a fixed value of b,

C is the number of clusters to be made ($2 \le C \le N$), and

f is an appropriate level of cluster fuzziness $f > 1$.

Then, the Euclidean distance between the i^{th} data point and the k^{th} cluster center with respect to the b^{th} dimension is calculated using the below equation:

$$D_{ikb} = \left\| \left(X_{ib} - CC_{kb} \right) \right\| \tag{3.3}$$

In equation (3.3), CC_{kb} is updated by updating the fuzzy membership matrix U according to D_{ikb} (if $D_{ikb} > 0$), as follows:

$$U_{ikb} = \frac{1}{\sum_{c=1}^{C} \left(\frac{D_{ib}}{D_{icb}} \right)^{f^2 - 1}} \tag{3.4}$$

This updating iteration is repeated until the changes in *U* are sufficiently small (such that $U \le \varepsilon$), where ε is a predefined termination criterion.

The conventional FCM algorithm requires estimations from the expert users to determine the number of clusters. Therefore, in this study a simple thresholding rule is proposed to automate the FCM clustering algorithm. To start with, an assumption is made in this study which limits the number of sub-fields to at most six. The FCM algorithm is executed iteratively starting with the assumption that each field contains maximum six sub-fields. After the first iteration, the Euclidean distances between the cluster centers are computed. If at least one distance stays below a defined threshold value, the number of sub-fields is decreased by one and the clustering operation is repeated with the reduced number of clusters. This iterative execution of the FCM clustering algorithm is carried out until all the

distances between the cluster centers stay above the threshold value. When the distances between the cluster centers stay below the selected threshold value, the resulting clustered image is selected to be the final clustered image and it is used in the further processing and analysis operations.

Let T is a threshold value, and D'_{ij} is the Euclidean distance among the cluster centers. Then, the thresholding procedure can be mathematically defined as follow:

If $D_{ij} \geq T$, then k is the appropriate cluster number.

$$D_{ij} = \left\| (CC_i - CC_j) \right\| \tag{3.5}$$

where $i=(1,2,...,k)$, $j=(1,2,...,k)$.

In this study, the automatic FCM clustering algorithm is carried out using the original image bands.

3.3.2. Refinement of the Clusters

The clustered image may contain noise and/or small clusters that may not correspond to true sub-fields. To overcome these limitations a sorting algorithm and a thresholding process have been proposed as well as performing morphological operations.

To start with, all the clusters that fall within the field being processed are sorted based on their sizes (the number of pixels falling within the cluster). The cluster sizes are computed based on the number of pixels that the clusters contain. Then, a ratio is computed by dividing the number of pixels within each cluster to total number of pixels that the field contain. With regard to computed ratios and the selected threshold value, those clusters with the ratio values that stay below the threshold value, are considered to be noise and removed. Next, to remove noise and fill the holes inside the clusters a simple morphological closing operation is performed for each cluster.

The closing of A (A is the binary desired image) by B (B is the square structure element) is obtained by the dilation of A by B, followed by erosion of the resulting structure by B:

$$A \cdot B = (A \oplus B) \ominus B \tag{3.6}$$

where, the dilation of A by the structuring element B is defined by:

$$A \oplus B = \cup_{b \in B} A_b \tag{3.7}$$

The erosion of the binary image A by the structuring element B is defined by:

$$A \ominus B = \{z \in E | B_z \subseteq A\} \tag{3.8}$$

where, B_z is the translation of B by the vector z, i.e., $B_z = \{b + z | b \in B\}, \forall_z \in E$.

For several example fields, the results of morphological operations as applied to output of FCM clustering are shown in Figure 3.3.

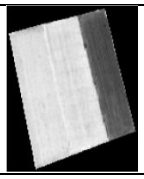		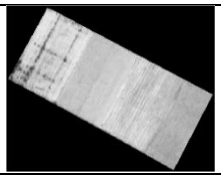	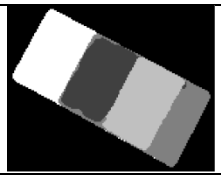
1-a) The Field Image	1-b) The Clustered Image	2-a) The Field Image	2-b) The Clustered Image
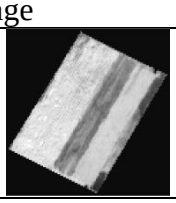	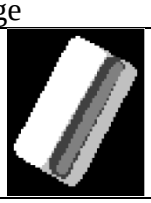	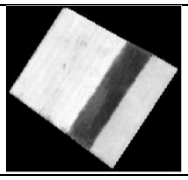	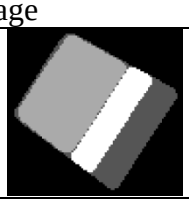
3-a) The Field Image	3-b) The Clustered Image	4-a) The Field Image	4-b) The Clustered Image

Figure 3.3. For the selected four sample fields, the results of clustering (after refinement step is conducted) the Quickbird PS satellite image.

3.4. Primary Contour Detection using the Improved Gradient Vector Flow (GVF) Snake Algorithm

Active contour models – known colloquially as snakes – are energy-minimizing curves that deform to fit image features [34]. Snakes lock on to nearby minima in the potential energy generated by processing an image. This energy is minimized by iterative gradient descent according to forces derived using variational calculus and Euler-Lagrange theory. In addition, internal (smoothing) forces produce tension and stiffness that constrain the behavior of the models; a supervising process or a user may specify external forces. As is the characteristic of gradient descent, the energy minimization process is unfortunately prone to oscillation unless precautions – typically the use of small time steps – are taken. Snakes do not try to solve the entire problem of finding salient image features; they rely on

other mechanisms to place them somewhere near a desired solution. For example, automatic initialization procedures can use standard image processing techniques to locate features of interest that are then refined using snakes. Even in cases where automatic initialization is not possible, however, active contour models can still be used for image interpretation. An expert user need only push a snake towards an image feature, and the energy minimization process will fit the model to the data.

3.4.1. Calculating the External and Internal Forces

There are many snake models and each was proposed for a purpose. One of the widely used and efficient snake models is the Gradient Vector Flow (GVF) Snake algorithm which is the improved model of the traditional snake. The GVF Snake has stronger convergence proficiency to boundary convexities and concavities than traditional snake [44]. The most important differences between snakes are in the energies that they use in order to deform the active contours.

A. Traditional Snake

Traditional snake is a controlled continuity curve under the influence of internal and external constraint forces.

The internal energy $E_{\text{int}}(k(s))$ can be written:

$$E_{\text{int}}(k(s)) = \frac{\alpha(s)|k_s(s)|^2 + \beta(s)|k_{ss}(s)|^2}{2} \tag{3.9}$$

where $k(s) = (x(s), y(s))$ is the curve of the snake, s is the parameter of the curve and $k_s(s)$, $k_{ss}(s)$ illustrate the first and second derivatives, respectively. The parameters α and β are weighting parameters that control the snake's tension and rigidity, respectively. The external energy function $E_{ext}(k(s))$ is derived from the image which attracts the snake (contour) to lines, edges and object boundaries. In other words, the external energy pushes the snake contour toward high or low intensity junction. The total energy can be expressed as a weighted combination of the energy that is derived from the image.

The general external energies are:

$$E_{ext}(k(s)) = -\left|\nabla I(k(s))\right|^2 \tag{3.10}$$

$$E_{ext}(k(s)) = -\left|\nabla I(G_\sigma(k(s)) * I(k(s))\right|^2 \tag{3.11}$$

Where, *I(k(s))* is a gray-level image, $G_\sigma(k(s))$ is a two-dimensional Gaussian function with standard deviation σ, and ∇ is the gradient operator. In this definition, it is clear that a larger σ will occasion the boundaries to become opaque and distorted. However, to use this, the external energy is minimized. Altogether, the snake model represents a compromise between the internal and external status via the weighting parameters.

B. Gradient Vector Flow (GVF) Snake

GVF Snake is an active contour model which uses vector field *V(k(s)) = (p(k(s)), q(k(s)))* to minimize the energy function that is computed for any image pixel *k(s) = (x(s), y(s))* :

$$\varepsilon = \iint \mu\left(p_x^2 + p_y^2 + q_x^2 + q_y^2\right) + \left|\nabla f\right|^2 \left|V - \nabla f\right|^2 dxdy \tag{3.12}$$

Where, ∇f is the gradient of the edge map, f is derived from the input image *I(k(s)),* μ is an adjustment parameter, and *dxdy* indicates partial derivatives with respect to *x* and *y* axes. After the minimization process, *V(k(s))* will be approximately zero where ∇f is larger (wherever the intensity changes significantly). The gradients are dispersed from heterogeneous areas to homogeneous regions. Active contours are composed of several connected nodes. Therefore, when these nodes are pushed toward object boundaries (field boundaries) based on gradient vectors lead to deform the active contours in order to delineate appropriate boundaries.

Although the above described energy model can solve some of the problems in boundary detection, it brings new difficulties. The main problem with the traditional model is the noise sensitivity: the greater the change in the gray levels, whether arising from noise or radiometric changes resulting from using high-resolution images, the larger the impact made by the snake on the energy function. This problem is more salient for the very high-

resolution images. Moreover, although edge image as an external force that gives rise to an accurate result around the edge lines, it may mislead the active contours toward noisy edges. Furthermore, it can decrease the convergence of the snake model. Indeed, the optimization schemes based on the gradient energies are very accurate around the edge areas, but their major drawback is their convergence radius.

To overcome the above-mentioned problems, a novel energy term based on the results of fuzzy c-means (FCM) clustering has been developed in this study. Since the clustering results are binary images, they have very good convergence energies in order to use them as the external energy in the snake algorithm. Besides, by virtue of their accuracy inside the clusters, which are the sub-fields, they considerably reduce the effect of edge noises inside the sub-fields that can mislead the initialized contours. In some cases, the clusters have low accuracies for the extraction of the exact sub-field boundaries. Furthermore, due to structure of the improved method the edge-based external forces are dominant near the edges. Accordingly, active contours around the sub-field boundaries, which are partially detected as the edge lines, evolve toward the real sub-field boundaries and cause to achieve accurate results.

In order to use the clusters as the external forces, the distance between each pixel and the cluster edge is calculated for each cluster using the Euclidean equation.

$$d = \sqrt{(x_2 - x_1)^2 + (y_2 - y_1)^2} \tag{3.13}$$

where, d is the Euclidean distance between $p_1 = (x_1, y_1)$ and $p_2 = (x_2, y_2)$, p_2 is any point (pixel) within the cluster, p_1 is the nearest point (pixel) of outside of the cluster to the point p_2.

Now, each pixel has a value showing its distance from the cluster's edge. Therefore, a matrix with the same size of the image is constructed which contain the distance values of the all pixels together. Then, the gradients of the matrix are calculated using equation 3.15 in two axes of the matrix (image) and the gradient vectors of the pixels are composed using the gradients in two dimensions. This process is performed for all clusters of the field being processed.

$$E_{exc}(k(s)) = -\left|\nabla I(k(s))\right|^2 \tag{3.14}$$

where $k(s) = (x(s), y(s))$ for each pixel of the image inside the selected cluster.

After calculating the gradients for each cluster, the gradient vectors are added to compose the cluster-based external force.

$$E_{cluster} = \sum_{i=1}^{n} E_i(k(s)) \tag{3.15}$$

where *n* is the number of clusters,

Finally, the total energy function is computed as:

$$E_{total} = E_{\text{int}} + E_{image} + E_{edge} + E_{cluster} \tag{3.16}$$

3.4.2. Automatic Initialization

The conventional snake algorithms are not automatic and require an expert for manually tracing the seed points. In order to automate the snake algorithm, a novel automatic seeding model has been proposed based on the results of FCM clustering. Since each cluster demonstrates a sub-filed, the clusters are used to initialize the improved GVF snake algorithm. To do that an ellipsoid is traced as the initial contour for each cluster using the geometrical properties of the cluster. In order to trace an ellipsoid, four main characteristics of the ellipsoid must be known. They are; 1- Center point, 2- Major axis length, 3- Minor axis length, and 4- Orientation angle of the ellipsoid.

1- Center point of the ellipsoid is the mass center of the cluster.
2- Major axis of the ellipsoid is the length (in pixels) of the major axis of the ellipse. It has the 45% length of the major axis of the cluster.
3- Minor axis of the ellipsoid is the length (in pixels) of the minor axis of the ellipse. It has the 45% length of the minor axis of the cluster.
4- Orientation of the ellipsoid is the angle (in degrees ranging from -90 to 90 degrees) between the x-axis and the major axis of the ellipse. It has the same angle between the major axis of the cluster and the x-axis of the image.

Figure 3.4.a shows one of the clusters obtained through automatic FCM clustering of the Ikonos image and an ellipse which was automatically traced to seed the snake algorithm.

Figure 3.4.b shows the same ellipse with the features indicated graphically. In Figure 3.4.b, the solid blue lines represent the major and minor axes, while the Green dots are the foci, and the orientation is the angle between the horizontal dotted line and the major axis.

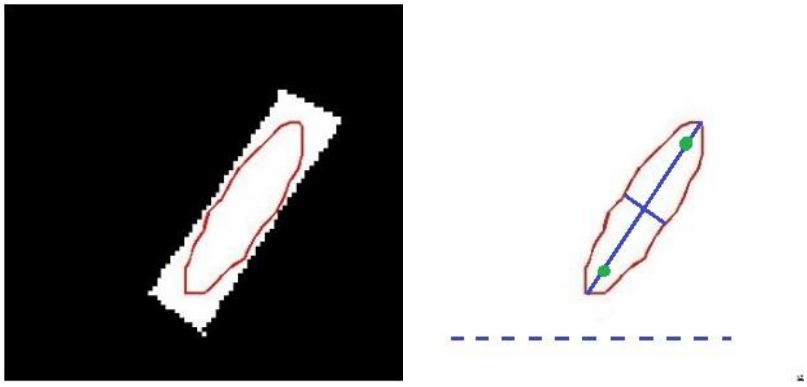

(a) (b)

Figure 3.4. (a) A cluster of the test field #13 obtained through clustering the Ikonos image and an automatically traced ellipse for seeding the contour, (b) the features of the ellipse.

After obtaining the main characteristics of the ellipse within a cluster, the coordinates of the points of the ellipse are calculated as follows:

$$x = x_c + \left(ma_1 \times \cos(\alpha) \times \cos(\beta) - ma_2 \times \sin(\alpha) \times \sin(\beta)\right) \tag{3.17}$$

$$y = y_c + \left(ma_1 \times \cos(\alpha) \times \sin(\beta) + ma_2 \times \sin(\alpha) \times \cos(\beta)\right) \tag{3.18}$$

where

$ma_1 = 0.45 \times MAL_1$, $ma_2 = 0.45 \times MAL_2$, $\alpha = p \times (\pi / 180)$, $p \in \{0,10,20,30,..,360\}$ (α expressed as radians), x_c is the coordinate of the cluster mass center in x axis, y_c is the coordinate of the cluster mass center in y axis, β is the minus orientation angle of the cluster in degrees, MAL_1 is the major axis of the cluster, and MAL_2 is the minor axis of the cluster.

The *x* and *y* coordinates are calculated for all *p* points. By connecting these points to each other, an ellipse is traced for each cluster falling within a field. Figure 3.5 illustrates the initialization procedure for the test field #13 using the QuickBird PS image.

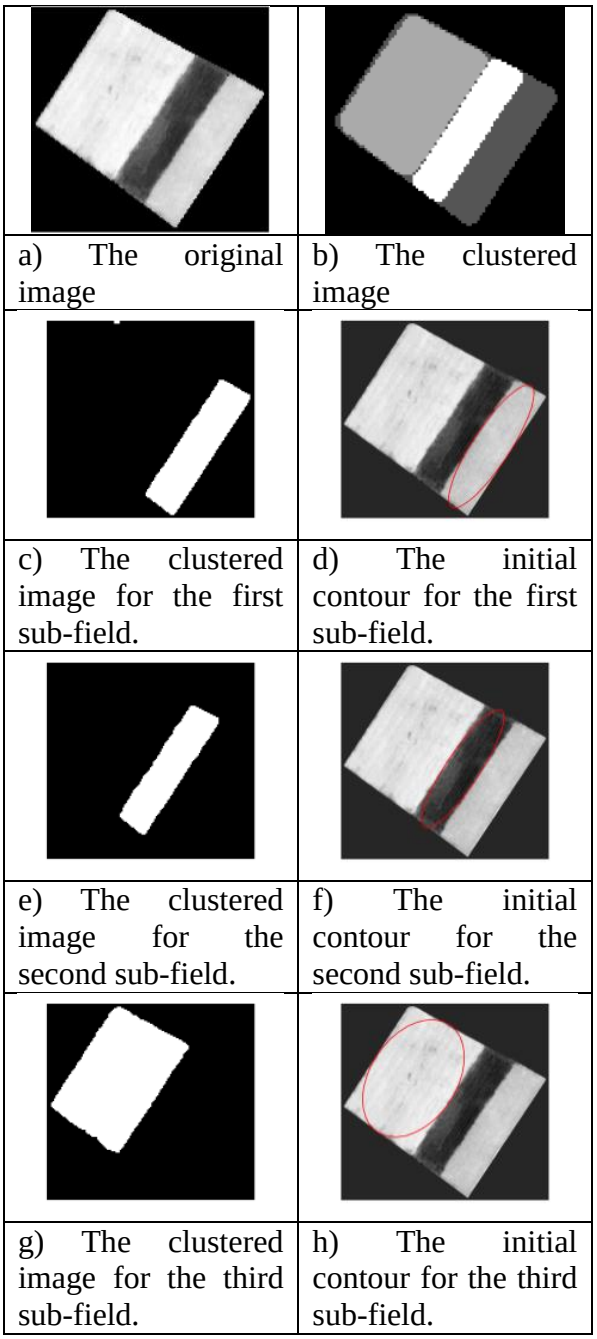

a) The original image | b) The clustered image

c) The clustered image for the first sub-field. | d) The initial contour for the first sub-field.

e) The clustered image for the second sub-field. | f) The initial contour for the second sub-field.

g) The clustered image for the third sub-field. | h) The initial contour for the third sub-field.

Figure 3.5. The illustration of the initialization procedure for the seeding procedure for field #13 using the QuickBird PS image.

3.4.3. The Execution of the Improved GVF Snake Algorithm

After generating the external and internal forces and initializing the snake algorithm for each cluster (sub-field), each seed contour starts to deform toward field boundaries independently. For each initial contour, the improved GVF snake is executed one contour at a time. For example, an agricultural field with three sub-fields requires three times

executions of the improved GVF snake. Figure 3.6 illustrates the evolving steps of the improved GVF snake algorithm for field #13 using the Quickbird PS image.

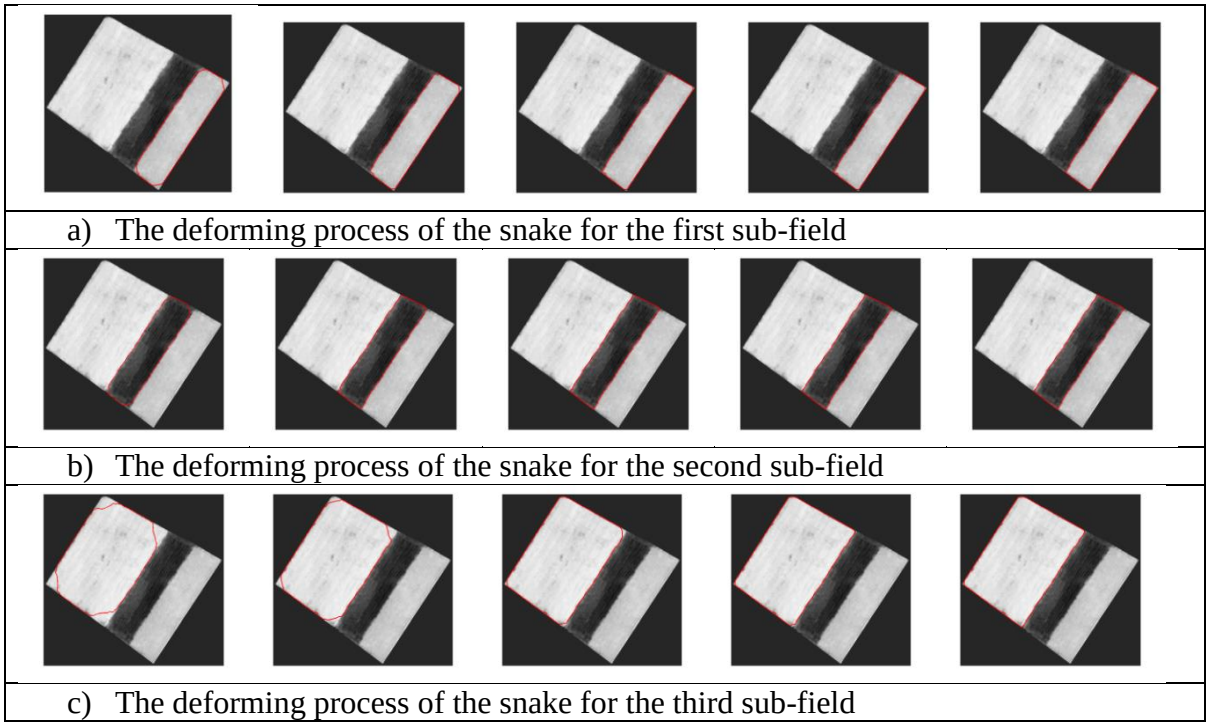

a) The deforming process of the snake for the first sub-field

b) The deforming process of the snake for the second sub-field

c) The deforming process of the snake for the third sub-field

Figure 3.6. The steps of the improved GVF snake for field #13 using the QuickBird PS image.

3.4.4. Boundary Masking

The output of the improved GVF snake algorithm contains the permanent field boundaries and the detected sub-field boundaries. As indicated earlier that the assumption made in this study that the permanent filed boundaries are known and stored in a GIS. Thus, these boundaries are excluded from further processing operations by means of a simple masking operation. Indeed, the main concern is to obtain the contours which represent the within field sub-boundaries. To do so, a buffer zone with a specified width is generated around the permanent field boundaries. The width of the buffer zone illustrates the distance from the permanent field boundaries. Therefore, the contours that reside inside the buffer zone are removed and only the contours that remain inside the agricultural field are used for further processing operations.

3.5. Line Simplification

The outputs of the snake algorithm after the boundary masking operation have three problems. The first problem is that there exist duplicate contours which belong to same sub-field boundary. This is due to applying the snake algorithm on clusters (sub-fields) one sub-field at a time. Therefore, duplicate lines may be generated on the boundaries of the adjacent sub-fields. The second problem is that the contours do not intersect with the permanent field boundaries. This is due to the prior step which eliminates either the contours or the parts of the contours inside the buffer zone around the permanent field boundaries. The third problem is that the contours are composed of several points that create a curved line rather than a straight line. However, the sub-boundaries should be straight-lines. Indeed, this problem is caused by the structure of the GVF snake algorithm, which moves each point toward the edges by considering external and internal forces independently without any force to push them to stay in a straight-line.

In order to overcome these limitations, a method with three steps has been developed. The steps of the method are as follows:

1- In order to reduce the duplicate contours to a single best contour, those contours that are closer to each other than a threshold value are determined and the average of the coordinates of the points of these contours are calculated. Eventually, the computed coordinates of the points are used to generate a single contour as the best-fit contour.
2- The contours obtained by virtue of the boundary masking operation float inside the field. Thus, these contours are extended to intersect the permanent field boundaries. However, a problem comes with the direction of the extension of the contours. To solve this problem, a line equation is calculated for each contour using the last three points of the contour. In addition, the line equations for the permanent boundaries are also calculated. Aftermaths, the intersection points and the distances between the contour lines and the permanent boundaries are computed. Finally, the contour line is extended towards the nearest intersection point and snapped to the permanent boundary.
3- Due to their structure, the active contours are composed of several connected points, which generally generate curved contours instead of straight lines. To achieve straight line segments, the detected line segments are simplified using the

Douglas-Peucker [45] algorithm, which is known to be a popular method for line simplification. The algorithm iteratively selects new points for inclusion in the thinned output polyline based on their deviation from a primary line connecting two neighbor points are already chosen for the inclusion. For the selected four fields, the results of a line simplification operation performed on the Quickbird PS satellite image are illustrated in Figure 3.7.

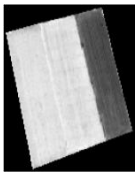	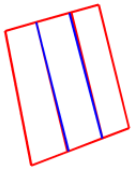	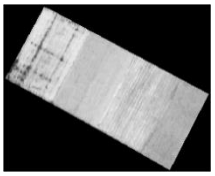	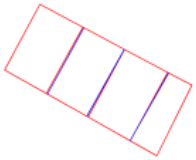
1-a) The Field Image	1-b) The Line simplification output.	2-a) The Field Image	2-b) The Line simplification output.
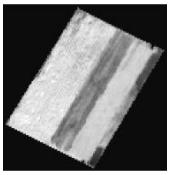	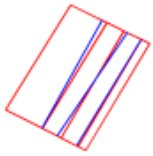	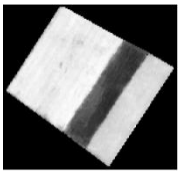	
3-a) The Field Image	3-b) The Line simplification output.	4-a) The Field Image	4-b) The Line simplification output.

Figure 3.7. For the selected four fields; (a) the Quickbird PS image and (b) the sub-boundaries (blue) after performing line simplification.

3.6. Forming the Sub-Polygons Within the Fields using a Recursive Algorithm

After the line simplification operation, the final within-field sub-boundaries are in the form of independent line segments. The sub-boundary line segments generally contain two or three points that include the end points of the segment. However, this information is not adequate for characterizing the closed sub-polygons (sub-fields) within the permanent boundaries of agricultural fields. Therefore, to construct sub-polygons, the connected line segments must be grouped in a way that each group defines an independent sub-polygon. This problem is known as “line to polygon conversion”. Several algorithms exist for

constructing polygons from the connected line segments. In general, these algorithms are based on region growing and shortest path techniques.

In this study, a simple recursive technique is used for reconstructing the polygons from the vogue line segments by utilizing a chain tree of the segments. A chain tree is constructed by considering the connectivity relations between the segments. The cycle paths, which start from a specific point and end in that point, is generated from this tree. Indeed, a cycle path from a point to itself composes of a polygon. Thus, considering that each point in this tree is a point of the line segment and this node has at least two connections to other nodes, which are known as the child nodes in tree structure, all the possible paths for each point can be found. Therefore, all the possible polygons that contain these points as vertices are determined. In each field, this process is repeated for all the vertex points that fall within the field. During composing the tree for one point as the root node, the cycle paths for other points are also determined because all possible paths are traced. Therefore, from a single tree, which is composed of considering a randomly selected point as root point, all the possible polygons can be traced and distinguished. This process is repeated until all the points of the line segments, involving in the tree, are selected as the root point.

First, a hash table is created for each point (node), containing the direct connection points. This is actually a different representation of the line segments detected. A set of connected segment group is obtained as the final result of the proposed method. For a sample field, the set and the corresponding hash table of the segments are illustrated in Figure 3.8.

<table>
<tr>
<td> 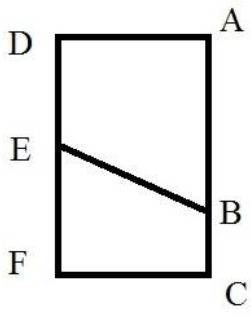
</td>
<td>MS = {([A-B], [B-C], [C-F], [F-E], [E-D], [B-E], [D-A])};</td>
<td>
<table>
<tr><th>Points</th><th>Connections</th></tr>
<tr><td>A</td><td>B,D</td></tr>
<tr><td>B</td><td>A,E,C</td></tr>
<tr><td>C</td><td>B,F</td></tr>
<tr><td>D</td><td>A,E</td></tr>
<tr><td>E</td><td>D,B,F</td></tr>
<tr><td>F</td><td>E,C</td></tr>
</table>
</td>
</tr>
<tr>
<td>a) Segmentation method result</td>
<td>b) All the available connected line segments</td>
<td>c) Hash table representation considering connections</td>
</tr>
</table>

Figure 3.8. The hash table for the connected segments in a sample field.

All the possible cycle paths can be found by composing a tree through the recursive algorithm for creating the nodes and its connections (children). The algorithm starts by selecting a point randomly form the hash table. Then, this point is passed to next process, making tree function, and all the nodes are recursively created from this root node. Figure 3.9 illustrates a tree constructed using point "A" as the root (major) node.

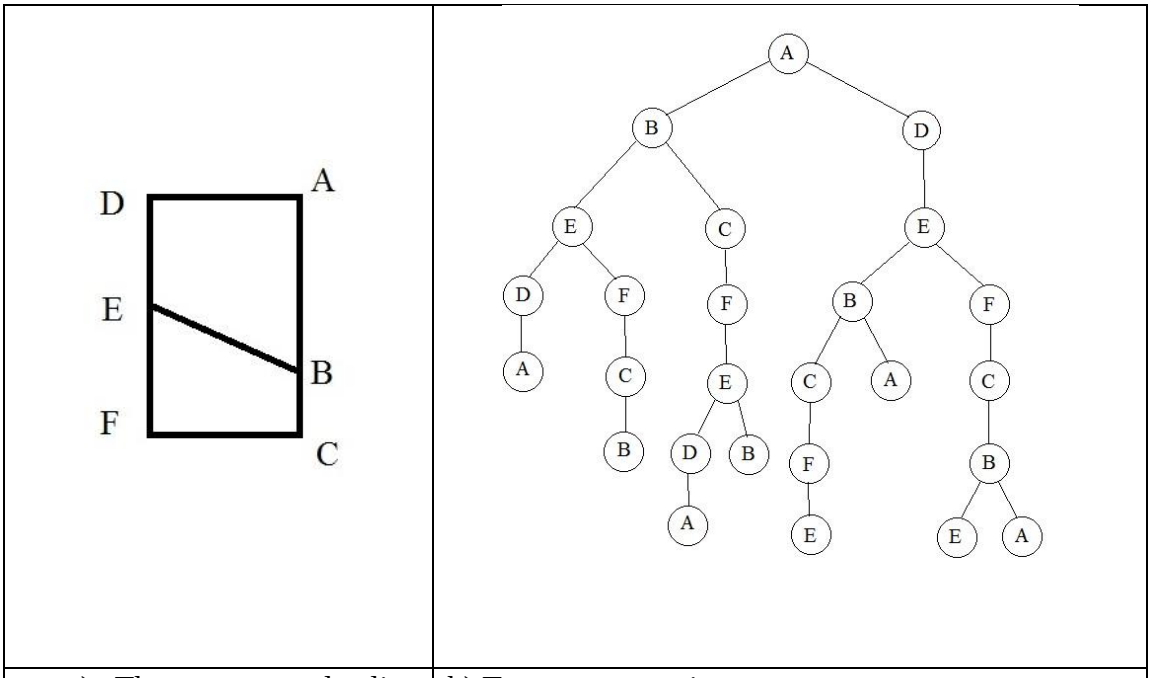

a) The connected line segments | b) Tree representation

Figure 3.9. All cycle paths for node A.

3.7. The Evaluation Methodology

The results were evaluated by comparing the geometry of the outputs of the proposed automatic sub-boundary detection method with the manually delineated sub-boundaries which are used as the reference data. The reference sub-field boundaries were manually delineated using the PCI Geomatica software in a previous study conducted by Turker and Ozdarici [16]. The methodology primarily is based on the overlaying of the field geometries extracted through the automatic segmentation procedure with the geometries of the manually segmented field geometries. Indeed, the concept is mainly based on the recognition of differences among the positional errors and the interpretation errors [46].

The match between two objects M_{ij} can be expressed as a geometrical mean of two conditional probabilities of M_i and M_j as follow:

$$\mathrm{M_{ij}} = \sqrt{\left(\mathrm{M_i}.\,\mathrm{M_j}\right)} \tag{3.19}$$

where

$$\mathrm{M_i} = {\mathrm{Area(i} \cap \mathrm{j)}}\Big/{\mathrm{Area(i)}} \tag{3.20}$$

$$\mathrm{M_j} = {\mathrm{Area(i} \cap \mathrm{j)}}\Big/{\mathrm{Area(j)}} \tag{3.21}$$

In Equation 3.20, M_{ij} gets a value between 0 and 1. If there is no matching at all M_{ij} equals 0, and if there is a complete match it equals 1. The matching percentages between the reference fields and the segmentation results, which were automatically extracted using the proposed method, are computed to evaluate the results. Considering all possibilities in the accuracy assessment procedure, the number of sub-fields detected through segmentation may not match with the number of truth sub-fields. Therefore, a matrix with the size of m × n is computed for each field. In the matrix, m represents the number of the truth sub-fields, while n represents the number of the result sub-fields. This matrix contains the values of the matching percentages for each of the truth sub-fields with each of the result sub-fields.

Due to calculation of the matching percentage values between the relevant truth sub-fields and the result sub-fields, each truth sub-field must be assigned to a separate result sub-field. However, here some problems may occur which can be solved by using distinct result sub-fields for each truth sub-field. Therefore, if a truth sub-field is associated with a result sub-field then, no more truth sub-field can also be associated with that result sub-field. Indeed, the key subject is to select the most appropriate pairs in order to satisfy the maximum sum of the matching area percentage. Eventually, the mean percentage values calculated using all the parcels provide the overall accuracy.

To illustrate the computation of the accuracy assessment method, all the evaluation procedures are discussed utilizing a sample field and are shown in Figure 3.10 [33]. There are four sub-fields in the truth and three sub-fields were extracted as the segmentation

result. T1, T2, T3 and T4 stand for truth sub-fields, whereas R1, R2 and R3 stand for the resulting sub-fields. Considering truth sub-field T1, the $M_{1,2}$ and $M_{1,3}$ matching percentage between these sub-fields become 0 because there is no overlapping area between R2 and R3 sub-fields. Consequently, $M_{1,2}$ and $M_{1,3}$ values equal to zero. Whereas there is overlap between T1 and R1 and calculated as $M_{1,1} = 0.89$. Furthermore, there are overlaps between T2 and R1, R2, while there is no overlap between T2 and R3; thus, the matching percentages are calculated as $M_{2,1}= 0.18$, $M_{2,2} = 0.91$ and $M_{2,3} = 0$. With regard to truth sub-field T3 has an overlap with R3, so for this sub-field the matching percentages are computed as $M_{3,1} = 0$, $M_{3,2} = 0$ and $M_{3,3} = 0.61$. Finally, matching percentages regarding truth sub-field T4 are $M_{4,1} = 0$, $M_{4,2} = 0$ and $M_{4,3} = 0.79$, illustrating only an overlap between T4 and R3, whereas there is no overlap considering R1 and R2 result sub-fields. Hitherto, the matching percentages among truth sub-fields and result sub-fields are calculated and the matching matrix is constructed. In the case of two matching percentage for an individual result sub-field the appropriate matching value determined using a simple threshold process, which the percentage value that stays above the specified threshold is accepted as the matching percentage. In this study, threshold value 75%, which was used in [26], is considered to verify the proposed segmentation outputs. Therefore, the matching percentage values are selected from the matching percentage matrix for those pairs that satisfy the threshold process as follows:

T1-R1: 0.89, T2-R2: 0.91, T4-R3: 79

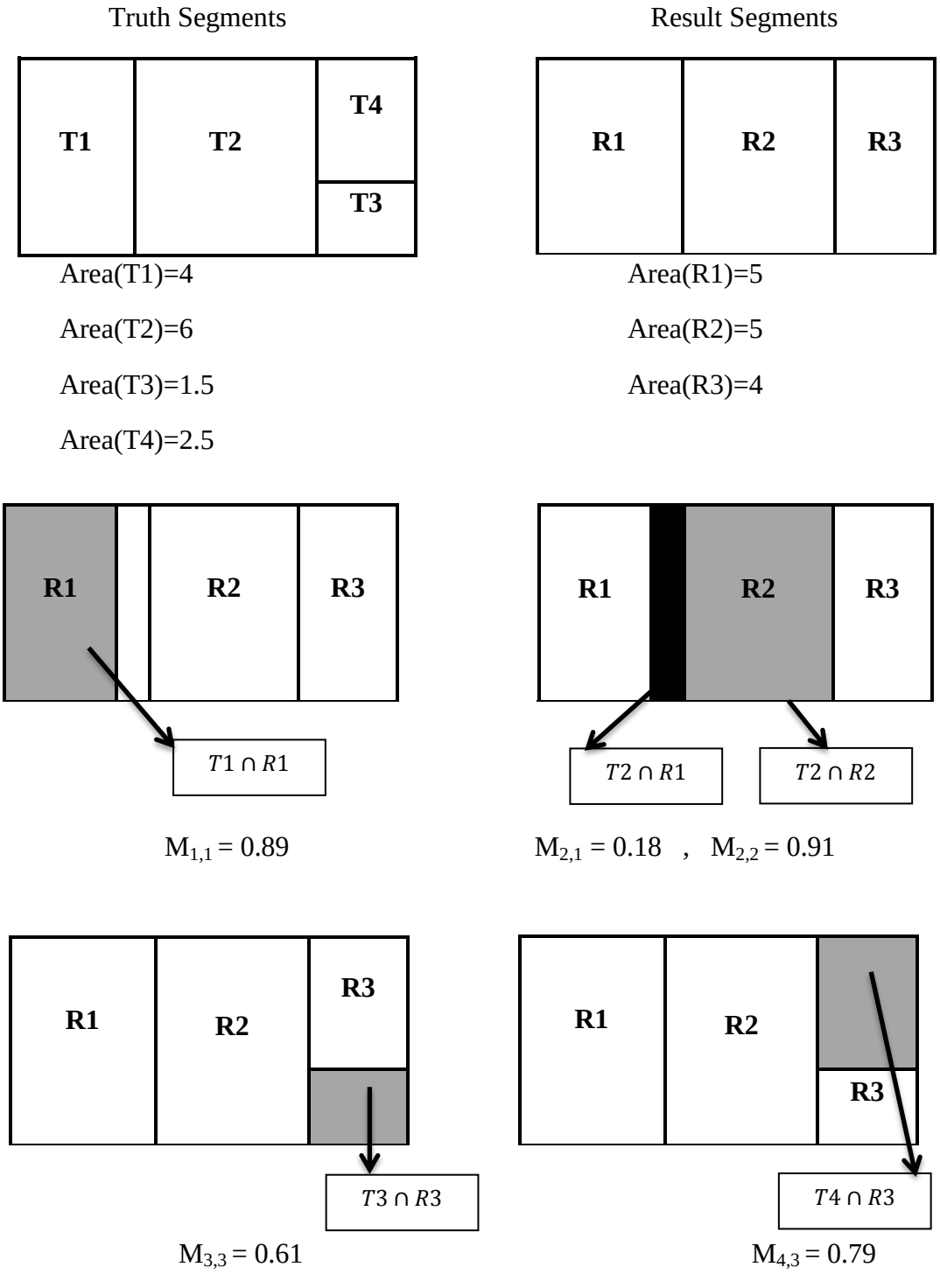

$$M = \begin{array}{c} \\ T1 \\ T2 \\ T3 \\ T4 \end{array} \begin{array}{c} \begin{array}{ccc} R1 & R2 & R3 \end{array} \\ \begin{bmatrix} 0.89 & 0 & 0 \\ 0.18 & 0.91 & 0 \\ 0 & 0 & 0.61 \\ 0 & 0 & 0.79 \end{bmatrix} \end{array}$$

Figure 3.10. For a simple field, the comparison of the geometries between the truth sub-fields (T1, T2, T3, T4) and the extracted result sub-fields (R1, R2, R3) [33].

Eventually, the mean value is computed as the overall accuracy for each field by dividing the sum of the matching percentage values by the number of truth sub-fields. Following this procedure, the overall accuracy for the example field given in Figure 3.10 is computed as:

$[(0.89+0.91+0.79)/4] = 0.648$

Hence, based on above computation the overall accuracy for the example field given in Figure 3.10 is computed to be 64.8 %.

4. Results and Analysis

4.1. Study Area

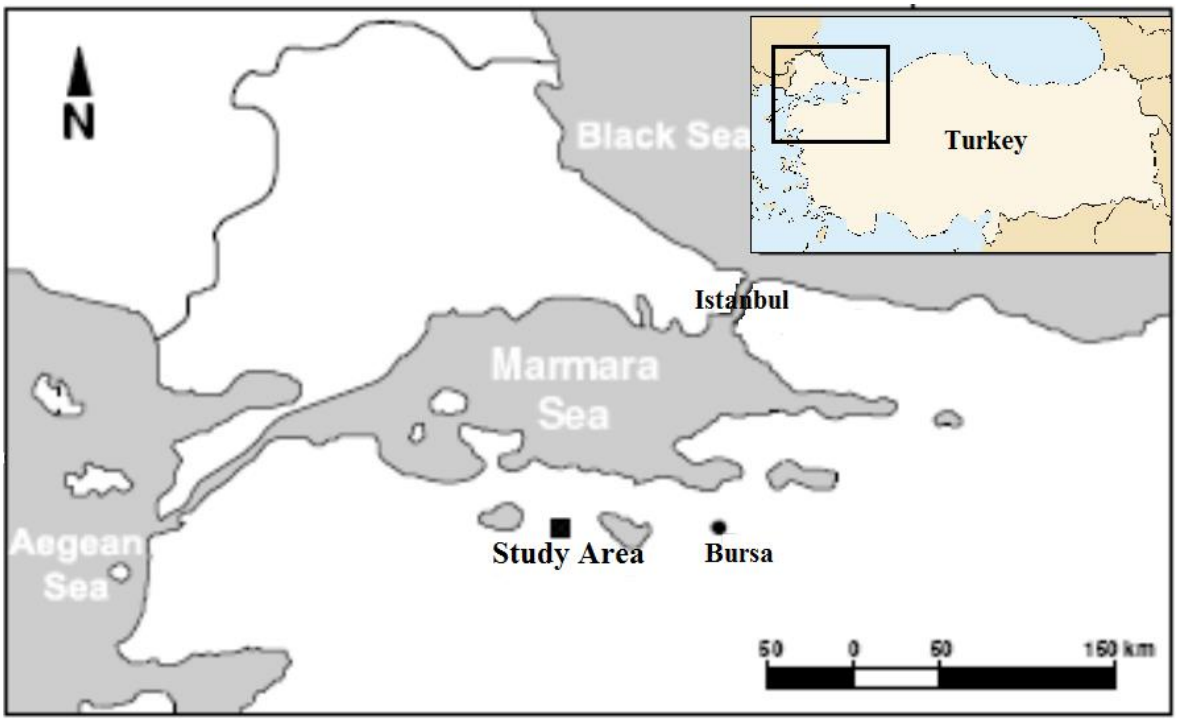

Figure 4.1. The location of the study area in Turkey

The study area is located in south-west of the town of Karacabey in Marmara region near Bursa situated in north-west of Turkey, covering approximately 4.6 km by 7.2 km. In the region, by virtue of the excellent weather conditions, agriculture is the primary land use. The agriculture land is utilized for the cultivation of a number of crops and several pasture fields for feeding animals. Tomato, corn, rice, sugar beet and pepper are the main crops grown in the region, where a land consolidation project was carried out between 1988 and 1992. The coordinates of the area of interest are 40º08´48´´to 40º12´42.4´´N and 28º14´14.2´´to 28º17´31´´E in UTM Zone-35.

Since the proposed within-field segmentation method is based on the integration of raster image and vector field boundary information, the execution requires two types of input data sets that are the raster image, and the vector data for the existing permanent field boundaries.

4.2. Data Sets

4.2.1. Raster Data

The high-resolution Ikonos Multispectral (XS) image, which was acquired in 15 July 2004, the high-resolution QuickBird XS image, which was acquired in 13 August 2004, and very high-resolution QuickBird Pansharpened (PS) image, which was acquired in 13 August 2004, were used as the raster data. Table 1 shows the important characteristics of the Ikonos and the QuickBird Satellite images.

Table 1. The spatial and spectral properties of the Ikonos and the QuickBird satellite images

Satellite	Spectral Bands	Spectral Range (μm)	Spatial Resolution (m)
Ikonos	Panchromatic	0.445 – 0.90	1
	B1: blue	0.45 – 0.52	4
	B2: green	0.52 – 0.60	4
	B3: red	0.63 – 0.69	4
	B4: near infrared	0.76 – 0.90	4
QuickBird	Panchromatic	0.49 – 0.90	0.61
	B1: blue	0.45 – 0.52	2.44
	B2: green	0.52 – 0.60	2.44
	B3: red	0.63 – 0.69	2.44
	B4: near infrared	0.76 – 0.90	2.44

4.2.2. Vector Data

The permanent field boundaries were available in digital vector form. The permanent field boundaries were digitized from the cadastral map sheets in a previous study conducted by [16]. The field boundaries were in UTM projection system. For each field, a formatted text file that involves the specific number, area, perimeter and other properties and the boundary coordinates were stored in a GIS database. In this study, the permanent field boundaries were used to intersect the detected sub-boundaries for constructing the sub-fields as well as using them as reference data for the evaluation of the results.

4.3. Results and Discussion

In this study, three types of images, which were acquired by the Ikonos and QuickBird satellite sensors, were used. The experimental tests were carried out on the normalized difference vegetation index (NDVI) images derived from these images. For each image, the results obtained are provided and their comparisons are given to discuss and analyze them. In this section, the results of the proposed automatic segmentation technique is demonstrated as well as providing a table of parameters and the parameter values used for the segmentation of the Ikonos and QuickBird images.

Throughout the method, several parameters and thresholds were needed to be defined. The threshold values are adaptable and can be changed by the user. The parameters and the parameter values which were used in this study are listed in Table 3. The parameter values defined for the Ikonos XS, QuickBird XS and QuickBird PS images are mainly dependent on the spatial resolution of the images. In this study, for each image, the values of the parameters were defined empirically after several trails. For example, the active contours do not change much with further evolutions after reaching the strong field boundaries. Therefore, to define iteration values for the parameters of the main improved GVF snake algorithm, initially the improved GVF snake algorithm was executed for a large iteration number. Then, the iteration values were selected, by looking at the deforming process step by step, for instance, five iteration at a time, during the evolution of the active contours.

The experimental tests of the proposed segmentation method were carried out on the selected 20 agricultural fields (Tables 7, 8, and 9). The test fields show diverse crop types and their adjacent properties, including different shapes and various sizes to analyze and demonstrate the superiority of the developed method. The sizes of the fields vary between 1.8 ha (field #14) to 18.9 ha (field #6). The number of sub-fields that each test field contains is between two and five (Table 2). Fields #2, #5, and #12 were particularly selected from the study area in order to test the performance of the approach on fields that contain sub-fields with the inner intersecting boundaries. On the other hand, the tests of the approach on fields that contain thin sub-fields were carried out on fields #7, #9, and #10. Indeed, this would be a challenging condition for testing the GVF Snake algorithm. Fields #19 and #20 were also good examples to illustrate the performance of the proposed approach. In these fields with the prolonged shape, one side of a field is much longer than the other side.

Table 2. The sizes and the number of sub-fields of the test fields.

Field ID	Area (ha)	Number of sub-fields	
		Ikonos	QuickBird
1	7.4	3	3
2	9.8	3	3
3	11.8	4	4
4	3.9	3	2
5	6.5	5	5
6	18.9	2	2
7	3.8	4	4
8	12.5	3	3
9	2.9	4	4
10	4.4	3	3
11	7.3	2	2
12	6.9	3	3
13	6.2	3	3
14	1.8	3	3
15	12	2	2
16	4.1	3	3
17	9.6	2	2
18	7.7	2	2
19	3.5	2	2
20	2.1	3	2

Table 3. The parameters and the values used for the Ikonos XS, QuickBird XS, and QuickBird PS images.

The Parameters/ Values	Ikonos XS	QuickBird XS	QuickBird PS
Edge detection: Canny			
- Low threshold	13	13	13
- High threshold	33	33	33
Clustering: Automated FCM clustering			
- Down Scale Percent (Reduce scale)	100%	75%	25%
- Fuzzy C-means clustering:			
- Number of clusters in each field	6	6	6
	0.8	1.5	2
- Distance between cluster centers	4 percent	4 percent	4 percent
- Cluster Area / Hole image area	6 pixels	6 pixels	6 pixels
- Morphological operation:			
- Close area within square			
Line segments analysis: Buffer zone			
- Buffer distance from each side of field boundary	3 pixels	2 pixels	2 pixels
Line segments analysis: Intersection			
- Distance between a line segment and the field boundary	6 pixels	6 pixels	6 pixels
Line simplification: Douglas-Peucker			
- Perpendicular offset	2 pixels	2 pixels	2 pixels
Line segments analysis: Merging segments			
- Distance between segment points	3 pixels	3 pixels	3 pixels
Snake:			
- Gradient minimizing:			
- regularization coefficient	0.2	0.2	0.2
- Iteration	80	80	80
- Initializing:			
- Initial ellipse major axis length	0.45	0.45	0.45
- Initial ellipse minor axis length	0.45	0.45	0.45
- Interpolation:			
- The maximum distance between two snake points	2	2	2
- The minimum distance between two snake points	0.5	0.5	0.5
- External forces:			
- Edge force coefficient	0.6	0.6	0.6
- Cluster force coefficient	0.72	0.66	0.66
- Internal forces:			
- Alpha (Elasticity)	0.05	0.05	0.05
- Beta (Rigidity)	0	0	0
- Gamma (Viscosity)	1	1	1
- Iteration	75	300	400

The overall accuracies for the detected within-field sub-boundaries for the Ikonos XS, QuickBird XS and QuickBird PS images are given in Table 4. As it can be seen in Table 4, the highest accuracy was provided by the Ikonos XS image with the computed overall accuracy of 93.61%. The overall accuracies for the QuickBird XS and QuickBird PS images were 84.96% and 88.78%, respectively. For the test fields used, the Ikonos image had lower within-field variations than the QuickBird images. Therefore, for the Ikonos image the FCM clustering algorithm generated better results with less noisy clusters, when compared with the QuickBird XS and QuickBird PS images. This prevents the proposed method from missing the sub-fields due to the seeding process, which is based on the results of clustering. Hence, the overall accuracy computed for the Ikonos XS image was higher than the overall accuracies computed for the QuickBird XS and QuickBird PS images.

Table 4. The overall accuracies computed for the Ikonos XS, QuickBird XS and QuickBird PS images.

Image	Overall Accuracy
Ikonos XS	% 93.61
QuickBird XS	% 84.96
QuickBird PS	% 88.78

The quantitative results that are categorized based on the quality of segmentation are given in Table 5, where equal segmentation means that the number of extracted sub-fields and the actual number of sub-fields are equal, over segmentation means that the number of extracted sub-fields are more than the actual number of sub-fields, and under segmentation means that the number of extracted sub-fields is less than the actual number of sub-fields. Of the total 20 test fields, the Ikonos XS, QuickBird XS, and QuickBird PS images provided 18, 13, and 15 fields with equal segmentation, illustrating a high ratio for the field-based segmentation performance of the proposed method. The best result for the equal segmentation category (18 out of 20) was provided by the Ikonos XS image. This is due to better clustering and the detected less noisy edges for this image. Indeed, as mentioned in the methodology section, the seeding process of the improved GVF Snake algorithm depends on the results of the automated FCM clustering to trace an ellipse for each sub-field. Thus, if the clustering operation does not find the true number of sub-fields, then the segmentation process would miss the sub-fields and the field may not be truly segmented. However, since the method is based on seeding each cluster individually, each

detected sub-field will have duplicate contours (see section 3.5) at the adjacent sub-boundaries. Therefore, a sub-field which is missed during clustering can be truly segmented using the sub-boundary of the extracted adjacent sub-field (cluster). Whereas the number of fields with the equal segmentation category, the number of fields with the over and under segmentation categories were significantly low. While the number of fields with over segmentation were 1, 1, and 2, the number of fields with under segmentation were 1, 6, and 3 for the Ikonos XS, QuickBird XS, and QuickBird PS images, respectively. Thus, the results of the under and over segmentation categories obviously demonstrate the reliability of the proposed method in terms of the field-based evaluation performance.

Table 5. The grouping of the segmentation results for the Ikonos XS, QuickBird XS, and QuickBird PS images.

Data sets		Ikonos	QuickBird XS	QuickBird PS
Segmentation grouping	Equal segmentation	18	13	15
	Over segmentation	1	1	2
	Under segmentation	1	6	3
Total		20	20	20

The quantitative results of the sub-boundaries detected were grouped based on the selected accuracy ranges (Table 6). Of the total 20 test fields, the Ikonos XS, QuickBird XS, and QuickBird PS images, respectively provided 17, 12, and 15 fields with the accuracy values of above 90%. These results illustrate the high reliability of the proposed method for delineating the within-field sub-boundaries in terms of the pixel-based performance assessment described in the evaluation methodology section (section 3.7). For the Ikonos XS image, a total of 17 fields out of 20 fell within the accuracy range of 90-100%, providing the best results of the images tested. This is believed to be due to better clustering and less noisy edges of the Ikonos XS image. The most effective factor for achieving accurate results through the proposed method is the external forces, which are computed based on the results of edge detection and clustering. Indeed, the edges provided dominant external forces around the boundaries. Therefore, the edge-based external forces mostly influence the active contours near the boundaries which are detected as the edges. On the other hand, if the true boundaries are not detected as the edges during edge

detection, this may drop the accuracies. However, in certain cases, the external force which was generated based on the clusters, refined the external force which was generated based on the edge image. Besides, the results of the automatic FCM clustering were the main reason for the accuracy values that stay below 70% since the actual sub-fields were not detected during the clustering procedure. Compared to number of fields that fall in the accuracy performance group of 90-100%, the number of fields that fall below the performance ratio of 90% is significantly low. Therefore, this clearly demonstrates the superiority of the proposed method for achieving accurate segmentation results for the fields that contain such challenging shapes, sizes, and within-field high variations.

The number of fields that fall in the accuracy performance group of 70-90% are 2, 2, and 1, respectively for the Ikonos XS, QuickBird XS, and QuickBird PS images. With regard to total number of fields that fall in the groups 70-90% and 90-100%, the proposed method is highly robust for the extraction of sub-boundaries. The number of fields that fall in the accuracy performance group of 50-70% are 0, 5, and 3, respectively for the Ikonos XS, QuickBird XS, and QuickBird PS images. Moreover, for each image only one field stayed within the accuracy performance group of 0-50%, clearly demonstrating the reliability of the proposed method, therefore.

Table 6. The accuracy grouping of the results obtained for the Ikonos XS, QuickBird XS, and QuickBird PS images.

Data sets		Ikonos XS	QuickBird XS	QuickBird PS
Accuracy grouping	%0 - %50	1	1	1
	%50 - %70	---	5	3
	%70 - %90	2	2	1
	%90 - %100	17	12	15
Total		20	20	20

4.3.1. The Results of the Ikonos Multispectral Image

The results of the Ikonos XS imagery with the outputs of the key steps are given in Table 7. As it can be seen in Table 7, the best result belongs to field #6 with the accuracy value of 99.92%. Although, for this field, the edge image contains some noisy edges near the permanent boundaries, by virtue of the accurate cluster output leads to almost 100% segmentation result, providing good external forces for the GVF Snake algorithm. Of the test fields, the lowest accuracy belongs to field #17 with the accuracy value of 47.84%.

Due to the extreme variation of the pixel brightness values in this field, several pixels were incorrectly clustered, giving rise to an extra seed ellipse (initial points) and resulting in incorrect segmentation of the sub-field. Fields #5, #7, #9 and #10 contain thin sub-fields, which are prolonged between the permanent field boundaries. Therefore, these fields are challenging cases for assessing the developed GVF snake algorithm because the active contours are expected to go through thin locations in order to reach the primary field boundaries during the deforming procedure. For fields #5, #7, #9, and #10, the proposed segmentation method provided the accuracies of 97.62%, 91.57%, 90.88% and 96.77%, respectively. Obviously, these results illustrate the reliability of the proposed method in such circumstances.

For fields #1 and #7, the output of edge detection was found to be under expectations. Indeed, the edge image did not correctly illustrate the sub-field boundaries. Nevertheless, due to the generated cluster-based external forces for the GVF Snake algorithm, the accuracy values in these fields reached to 97.9% and 91.57%, respectively. But, fields #2, #3, #10, and #16 contained incorrectly clustered pixels and therefore provided inaccurate clustering results. Nevertheless, due to external forces generated from the edge image, the initial contours truly and precisely caught the correct sub-field boundaries and provided accurate segmentation results for these fields. Besides, considering the edge images of field #8, and fields #11 to #19, the extraction of sub- boundaries is challenging and even the sub-boundaries cannot be distinguished if only the edge image is considered. But, using both the clusters and the edge image as the external forces pushed the contours to accurate boundaries in these cases (Table 7). Further, the buffer zone generated around the permanent field boundaries as well as the steps followed for intersecting sub-boundaries with the permanent field boundaries provide accurate results for the segments near the permanent field boundaries.

The reliability of the proposed method is also illustrated with the results of fields #2, #4 and #12, in which a sub- boundary intersects with another sub-boundary (inner intersection boundaries) making the within-field segmentation process more challenging. Fields #19 and #20 are the good examples to illustrate the performance of the proposed method. In these fields with the prolonged shape, one side of a field is much longer than the other side. However, the computed accuracy values of 99.61% and 99.37% respectively for these fields clearly demonstrate the superiority of the proposed segmentation method.

In addition to accuracy results of the detected sub- boundaries (Table 7), the crop types of the sub-fields are also included in the analysis and discussion of the results considering the class types of the sub-fields. The crop types of the sub-fields were determined by visiting the fields on the ground for the previous study conducted by [16].

With regard to crop types, the sub-fields are grouped into ten classes: 1-Tomato, 2-Corn, 3-Residue, 4-Onion, 5-Sugar Beet, 6-Orchard, 7-Pepper, 8-Rice, 9-Clover, and 10-Plowed. As it can be seen in the results provided in Table 7, the proposed segmentation method efficiently and accurately distinguished the segments for most of the class combinations of the adjacent sub-fields. Nevertheless, the most challenging fields for performing the segmentation were those that contain the class combinations of corn and clover, corn and rice, and tomato and clover. The adjacent class combinations of corn and rice have led to lower accuracy results when compared with the other adjacent class combinations. Indeed, the similar spectral reflectance characteristics of the adjacent sub-fields give rise to mislead the clustering step of the automated FCM algorithm and cause the incorrect labeling of these diverse clusters with the same label. Thus, the cluster-based external force and the seeding of the improved GVF snake algorithm in the segmentation process may become incorrect and would lead to low accuracy performance in these circumstances.

Of the sub-field classes, the most distinguishable one is residue (#3) which was accurately segmented using the proposed method regardless of the size, shape, and the adjacency properties of the within field sub-fields. For fields #2, #3, #8, #10, #15, #16, and #17, the results demonstrate that, rice and, in some cases, corn and sugar beet do not have good inner clustering results. However, due to the cluster refinement process and the subsequent novel seeding steps, these problems have mostly been solved for fields #2, #3, #8, #10, #15 and #16, providing the accuracy values of 97.58%, 98.66%, 77.11%, 96.77%, 99.52%, 87.24% and 99.56%, respectively. These results also clearly demonstrate the reliability of

the proposed method in such challenging conditions. The low accuracy value computed for field #17 is thought to be due to within-field large variation which gives rise to an extra seeding step and clustering this class incorrectly into two separate classes and generating two sub-fields, therefore. Hence, field #17 was segmented into three sub-fields instead of two.

Table 7. For the Ikonos XS image, the computed NDVI image, the extracted edges, the clustering results, the permanent field boundaries (red), the extracted sub-field boundaries (blue), and the accuracies of the test fields. (1-Tomato, 2-Corn, 3-Residue, 4-Onion, 5-Sugar Beet, 6-Orchard, 7-Pepper, 8-Rice, 9-Clover, 10-Plowed).

ID	NDVI Image	Edge Image	Clustered Image	Field Boundaries	Accu-racy (%)
1	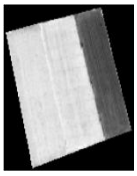	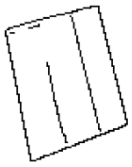		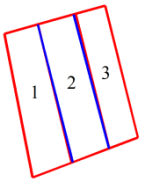	97.9
2	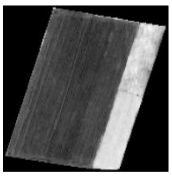	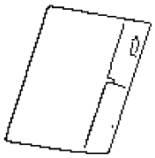		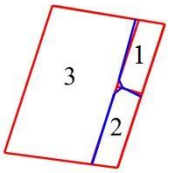	97.58
3	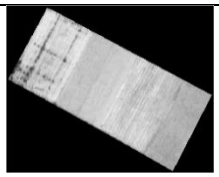	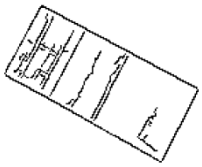	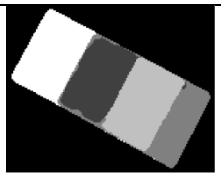	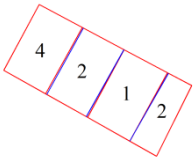	98.66
4	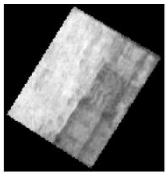		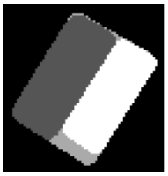	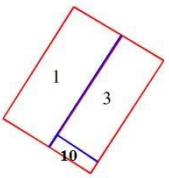	97.62
5	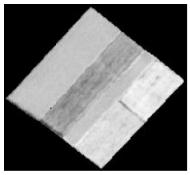	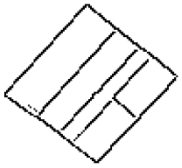	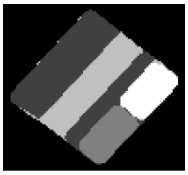	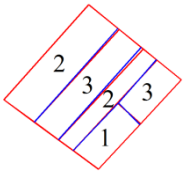	97.65

Table 7. Continued.

ID	NDVI Image	Edge Image	Clustered Image	Field Boundaries	Accu-racy (%)
6	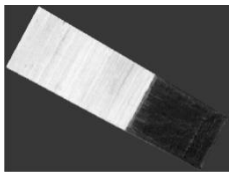	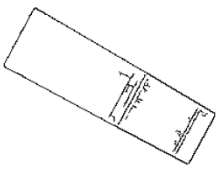	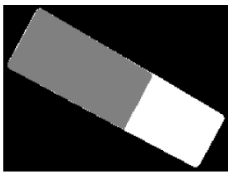	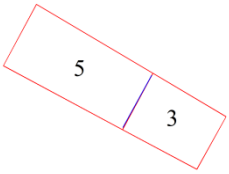	99.92
7	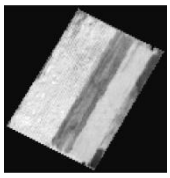		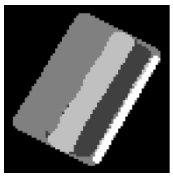	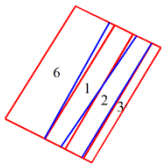	91.57
8	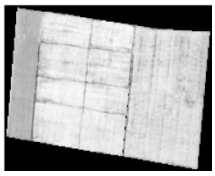	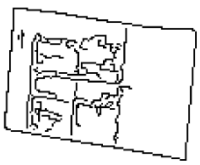		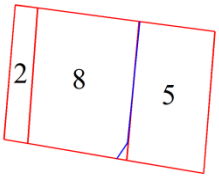	77.11
9	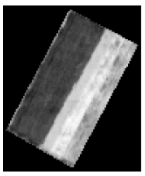	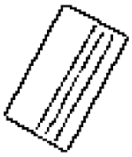	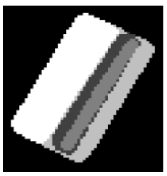	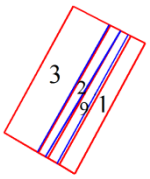	90.88
10	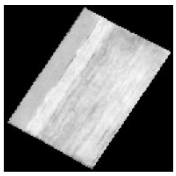		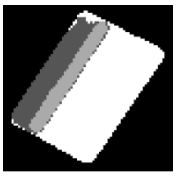	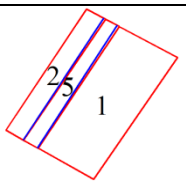	96.77
11	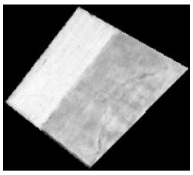		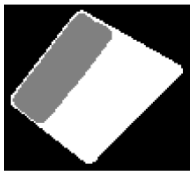	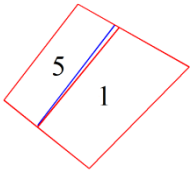	99.31
12	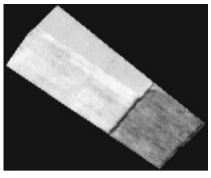	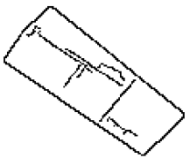	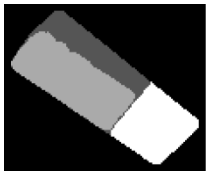	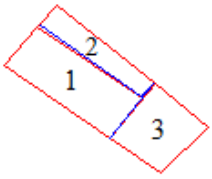	98.90

Table 7. Continued.

ID	NDVI Image	Edge Image	Clustered Image	Field Boundaries	Accu-racy (%)
13	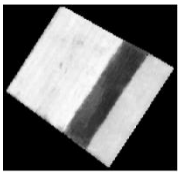	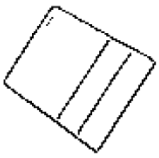	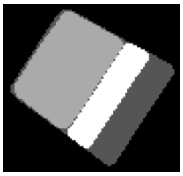	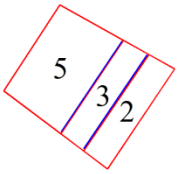	97.64
14				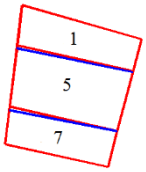	97.96
15	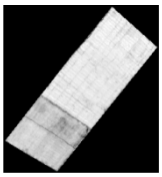			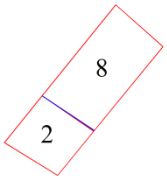	99.52
16	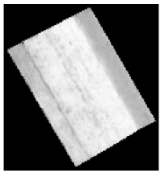		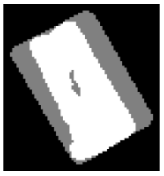	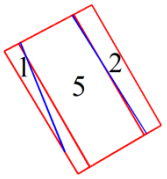	87.24
17				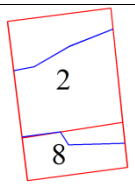	47.84
18	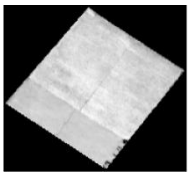		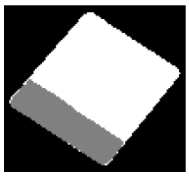	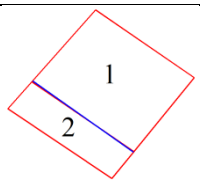	99.21
19				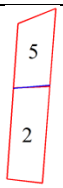	99.61

Table 7. Continued.

ID	NDVI Image	Edge Image	Clustered Image	Field Boundaries	Accu-racy (%)
20				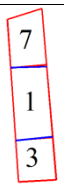	99.37
Overall accuracy					93.61

4.3.2. The Results of the QuickBird Multispectral Image

The results of the QuickBird XS imagery with the outputs of the key steps are given in Table 8. As it can be seen in Table 8, field #17 provided the best result with the accuracy value of 99.66%. Even though, for this field, the result of the automatic FCM clustering contains noisy clusters inside the sub-fields, by virtue of the accurate edge detection the final accuracy is almost 100%, illustrating the effect of the external forces for the GVF Snake algorithm.

Of the test fields, the lowest accuracy performance belongs to field #9 with the accuracy value of 41.28%. This is due to the fact that a number of pixels with similar brightness values that fall within the neighboring sub-fields were incorrectly clustered, giving rise to miss actual sub-fields in the clustering process and the following seeding steps of the GVF snake algorithm.

Fields #5, #7, #9 and #10 contain thin sub-fields, which are prolonged between the permanent field boundaries. Therefore, these fields are challenging cases for testing the developed GVF snake algorithm because the active contours are expected to go through thin locations in order to reach the primary field boundaries during the deforming process. Since the proposed segmentation approach uses the results of clustering as an additional external force along with the common external forces for the GVF Snake algorithm, the evolution of the active contours toward true boundaries is more efficient. However, in these fields, due to similar brightness values of the pixels, the automatic Snake seeding

method is misled because of the incorrect clustering results. Accordingly, the computed accuracy values of 66.49%, 65.29%, 41.28% and 65.79% for these fields have become lower than the accuracy values computed for the other fields.

For fields #1, #2 and #3, the output of edge detection was found to be under expectations. Indeed, the edge image did not correctly illustrate the sub-field boundaries. However, due to the proposed cluster-based external forces for the GVF Snake algorithm, the computed accuracy values for these fields reached to 94.49%, 96.16% and 88.34%, respectively, demonstrating the reliability of the proposed method in such conditions. However, fields #6, #16 and #17 contained incorrectly clustered pixels and therefore, they did not provide accurate clustering results. Nevertheless, due to external forces generated from the edge image, the initial contours truly and precisely caught the correct sub-field boundaries and caused accurate segmentation results for these fields.

Considering the edge images of fields #4, #10 to #14 and #20, the extraction of sub-boundaries is challenging and, in some cases, the sub-boundaries cannot be distinguished using the edge image only. However, for these fields, with the use of both the clusters and the edge image as the external forces, the contours were pushed toward correct boundaries (Table 8). Further, the buffer zone generated around the permanent field boundaries and the steps followed for the intersection of sub-boundaries with the permanent field boundaries have provided accurate results for those segments that stayed close to permanent field boundaries.

For fields #3, #5, #8, #15 and #18, neither the edge image nor the clustering results were quite accurate individually to achieve segmentation with high accuracy. Fields #3, #15 and #18 are good examples for illustrating the efficiency of the proposed seeding method. In these fields, the results are accurate despite the fact that the clustering results are not quite correct. The accuracy values for these fields were computed as 88.34%, 99.54% and 98.42%, respectively. Nevertheless, in fields #5 and #8 some sub-fields were not able to be seeded due to inaccurate clustering results. In addition, the edge images also contained the noisy edges. Consequently, these fields have provided lower accuracy values in comparison with the other fields.

Fields #19 and #20 are good examples to illustrate the performance of the proposed approach. In these fields with the prolonged shape, one side of the field is much longer than the other side. Despite this fact, the computed accuracy values for these fields were

99.22% and 99.11%, respectively demonstrating the superiority of the proposed segmentation approach.

In addition to accuracy values of the detected sub boundaries (Table 8), the crop types (class types) of the sub-fields were also included in the analysis and discussion of the results. As it can be seen in Table 8, the proposed segmentation approach efficiently and accurately distinguished the segments for most of the class combinations of the adjacent sub-fields. Nevertheless, the most challenging fields for performing the segmentation were those that contain the class combinations of corn and clover, corn and rice, and tomato and clover. Further, in a few cases the class combinations of tomato and corn, tomato and residue, and sugar beet and rice have also lead to lower accuracy values. Indeed, the similar spectral reflectance characteristics of these classes within the adjacent sub-fields have given rise to mislead the automatic FCM clustering and have caused the incorrect labeling of these diverse clusters with the same label. Thus, the generation of the cluster-based external forces and the novel seeding for the improved GVF snake algorithm for the segmentation process have become incorrect and this have led to lower the accuracy values in these circumstances.

Of the sub-field class types, residue was the most distinguishable class. Residue was accurately segmented using the proposed approach regardless of the size, shape, and the adjacency properties of the within-field sub-fields. The results obtained for fields #3, #8, #10, #16 and #17 demonstrate that, rice, onion and sugar beet, and in some cases corn caused the noisy clustering results. However, due to cluster refinement process and the subsequent novel seeding steps, which were developed in this study, these problems have mostly been solved for fields #3, #16, and #17, providing 88.34%, 98.08%, and 99.66% accuracies, respectively. Therefore, these results also clearly demonstrate the reliability of the proposed method in such challenging conditions. The low accuracy values computed for field #10 is due to within field extreme variation of the class tomato, which gives rise to an extra seeding step causing the incorrect clustering of this field into two separate classes. Thus, field #10 was segmented into four sub-fields instead of three.

Table 8. For the QuickBird XS image, the computed NDVI image, the extracted edges, the clustering results, the permanent field boundaries (red), the extracted sub-field boundaries (blue), and the accuracies of the test fields. (1-Tomato, 2-Corn, 3-Residue, 4-Onion, 5-Sugar Beet, 6-Orchard, 7-Pepper, 8-Rice, 9-Clover).

ID	NDVI Image	Edge Image	Clustered Image	Field Boundaries	Accu-racy (%)
1	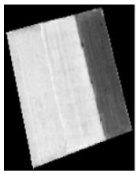	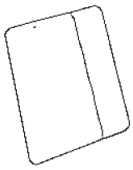	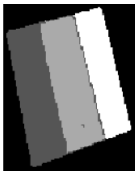	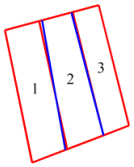	94.49
2	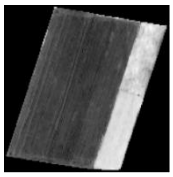	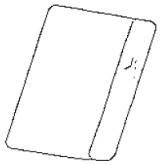	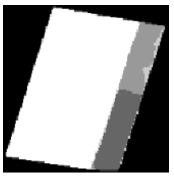	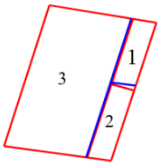	96.16
3	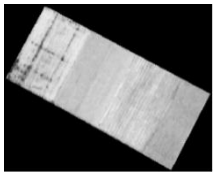	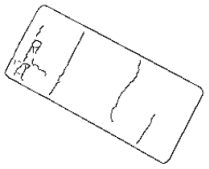	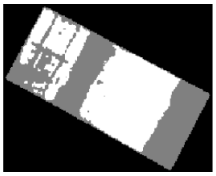	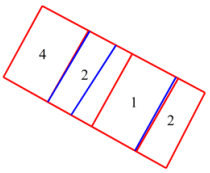	88.34
4	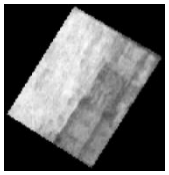			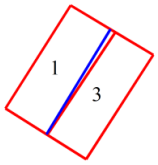	96.70
5	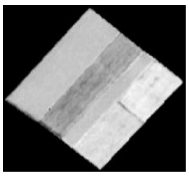	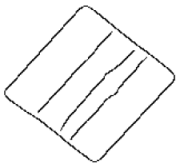	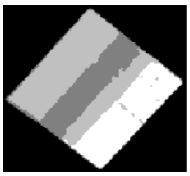	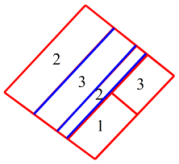	66.49
6	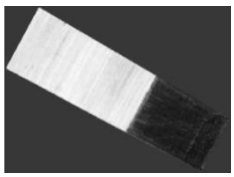	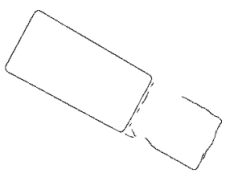	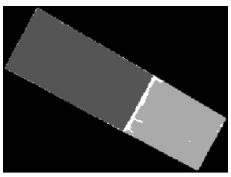	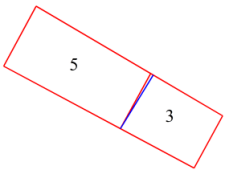	99.23

Table 8. Continued.

ID	NDVI Image	Edge Image	Clustered Image	Field Boundaries	Accu-racy (%)
7	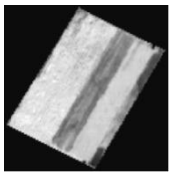	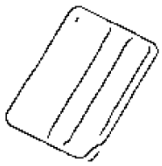		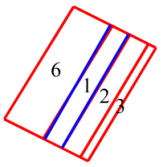	65.29
8	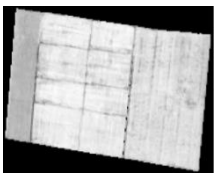	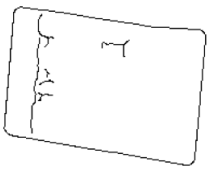	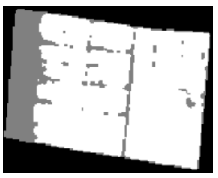	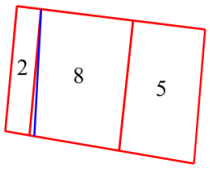	57.53
9	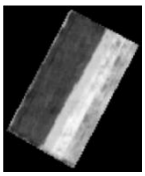	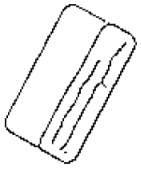	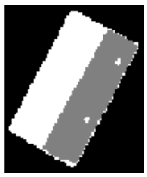	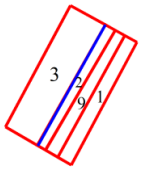	41.28
10	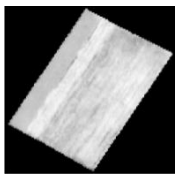	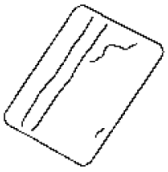	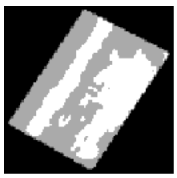	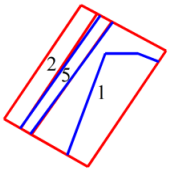	65.79
11	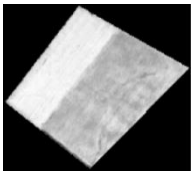	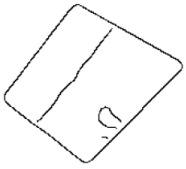	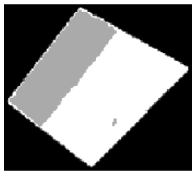	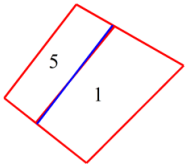	99.12
12	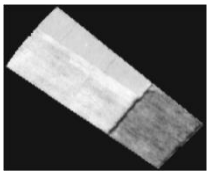	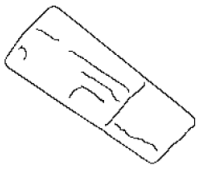		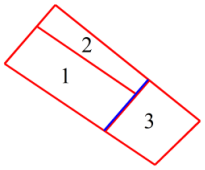	79.10
13	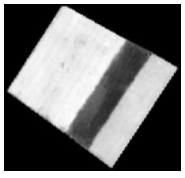	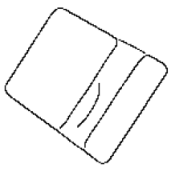	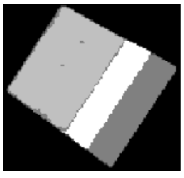	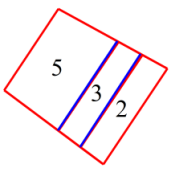	97.36

Table 8. Continued.

ID	NDVI Image	Edge Image	Clustered Image	Field Boundaries	Accu-racy (%)
14				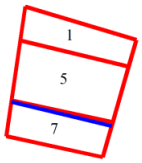	58.36
15	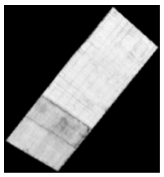	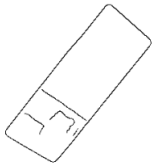	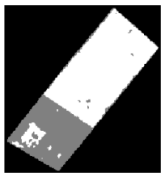	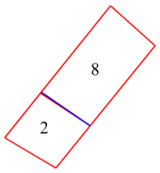	99.54
16	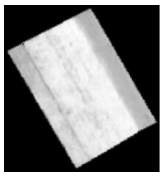	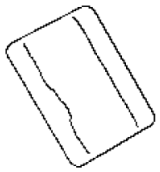	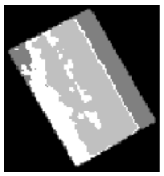	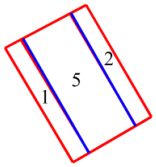	98.08
17	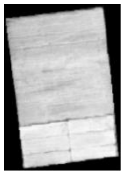			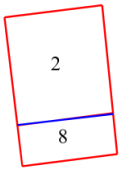	99.66
18	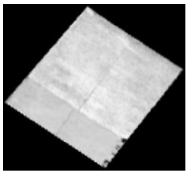	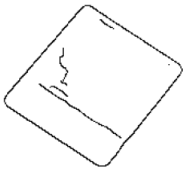	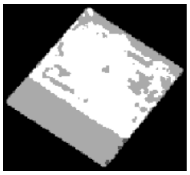	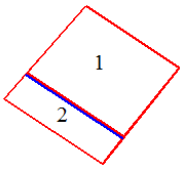	98.42
19				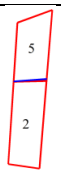	99.22
20					99.11
Overall accuracy					84.96

4.3.3. The Results of the QuickBird Pansharpened Image

The results of the QuickBird Pansharpened (PS) imagery with the outputs of the key steps are given in Table 9. As it can be seen in Table 9, the best result belongs to field #6 with the accuracy value of 99.90%. Even though, the automatic FCM clustering generated three clusters instead of two true clusters for this field, the final accuracy value was almost 100%. It is believed that the elimination of small clusters and the accurate result of the edge detection were the main causes for the high accuracy. Indeed, as was the case in this field, the cluster refinement and the edge detection steps provide good external forces for the improved GVF Snake algorithm which leads to accurate image segmentation result. Of the test fields, the lowest accuracy was provided by field #3 with the accuracy value of 49.85%. It is evident that the extreme variations of the pixel brightness values in this field have caused the incorrect clustering of the pixels into several separate clusters. Therefore, the seeding process of the improved GVF snake algorithm was misled and caused the incorrect segmentation of the sub-field.

Fields #5, #7, #9 and #10 contain thin sub-fields, which are prolonged between the permanent field boundaries. Therefore, these fields are challenging cases for testing the developed GVF snake algorithm because the active contours are expected to go through thin locations in order to reach the primary field boundaries during the deforming procedure. Since the proposed segmentation approach uses the clustering results as the additional external forces along with the common external forces for the GVF Snake algorithm, the evolution of the active contours toward true boundaries becomes easier and more efficient in such cases. However, the automatic Snake seeding method was misled due to similar pixel values in these fields. Accordingly, the accuracies for fields #5 and #9 (64.98% and 56.15%, respectively) are relatively low when compared to other fields. However, the accuracy values of 91.05% and 94.63% computed for fields #7 and #10, respectively were significantly high. Obviously, the results illustrate the efficiency of the proposed segmentation approach for such fields, in which the clustered image and the edge image do not include significant noise.

For fields #1, #2, #4, #10, #12, #18 and #19 the results of the edge detection are under expectations. Indeed, the edge images generated for these fields do not closely match the true sub-boundaries. However, due to the generated cluster-based external forces for the GVF Snake algorithm the accuracy values reached to 97.99%, 98.71%, 99.07%, 94.63%,

79.41%, 98.92%, and 98.97, respectively for these fields. Therefore, for these fields the computed accuracy values clearly show the reliability of the proposed method in such circumstances.

A significant amount of incorrectly clustered pixels were evident in fields #16 and #17 illustrating low clustering accuracy. However, due to external forces generated from the edge image, the initial contours truly and precisely caught the correct sub-field boundaries and caused the accurate segmentation of these fields. Moreover, considering the edge images generated for fields #4, #10 - #14, and #20, the extraction of sub-boundaries is very challenging and even, in some cases, the sub-boundaries cannot be distinguished using the edge images only. But, with the use of both the clusters and the edge image as the external forces the contours were pushed toward accurate boundaries in these fields (Table 8). Further, the buffer zone generated around the permanent field boundaries as well as the intersection steps followed in the proposed approach provided accurate results.

Moreover, it is evident that neither the edge image nor the results of clustering is not reliable enough individually for fields #3, #5, #8, #10, #14, and #15 to generate accurate external forces for the improved GVF snake algorithm during evolution of the active contours. Of these, fields #8, #10 and #15 are good examples to illustrate the efficiency of the proposed seeding approach. For these fields, the accuracy values of 96.37%, 94.63% and 99.86%, respectively are very high despite the fact that the clustering results are not quite accurate. Nevertheless, in fields #5 and #8 some actual sub-fields were not seeded due to inaccurate clustering results. Thus, the proposed approach have not recognized the correct sub-fields in order to generate the seed contours. In addition, the generated edge image also contained several noisy edges. Thus, the accuracy values computed for these fields have become relatively low when compared to the other fields.

Fields #19 and #20 are good examples to illustrate the performance of the proposed method. In these fields with the prolonged shape, one side of a field is much longer than the other side. Despite their prolonged shape however, the computed accuracy values for these fields were 99.22% and 99.11%, respectively demonstrating the superiority of the proposed segmentation approach therefore.

In addition to accuracy results of the detected sub-boundaries (Table 9), the crop types (class types) of the sub-fields are also included in the analysis and discussion of the results. As it can be seen in Table 9, the proposed segmentation approach efficiently and

accurately distinguished the segments for most of the class combinations of the adjacent sub-fields and correctly extracted the sub-fields. Nevertheless, the most challenging fields for the proposed method to perform segmentation were those that contain the class combinations of corn and clover, corn and rice, and tomato and clover. However, the adjacent class combination of tomato and corn have led to lower accuracy results when compared with the other adjacent class combinations. Indeed, the similar spectral reflectance characteristics of the classes of the adjacent sub-fields give rise to mislead the clustering step of the automated FCM algorithm and cause the labeling of these diverse clusters with the same label. Hence, the generated cluster-based external forces and the seeding of the improved GVF snake algorithm in the segmentation process would not be correct and would lead to low accuracy values in these circumstances.

Of the sub-field class types, residue was the most distinguishable class type. It is evident that the sub-fields that contain residue were accurately segmented using the proposed approach regardless of the size, shape, and the adjacency properties of the sub-fields contained within a field. The results obtained for fields #3, #8, #10, #16 and #17 demonstrate that, rice, onion, sugar beet and, in some cases, corn do not have good clustering results. However, due to the implementation of the cluster refinement process and the developed novel seeding steps, these problems have mostly been solved for fields #8, #10, #16 and #17 providing the accuracy values of 96.37%, 94.63%, 95.79%, and 99.56%, respectively. These results also clearly demonstrate the reliability of the proposed method in such challenging conditions. The low accuracy value computed for field #3 is thought to be due to within-field large variation of the class onion contained within. Thus, the area covered by the class onion in the field was incorrectly clustered into two classes leading to an extra seeding step and separating the onion covered area into two sub-fields. As a result, field #3 was segmented into five sub-fields instead of true four sub-fields.

Table 9. For the QuickBird PS image, the computed NDVI image, the extracted edges, the clustering results, the permanent field boundaries (red), the extracted sub-field boundaries (blue), and the accuracies of the test fields. (1-Tomato, 2-Corn, 3-Residue, 4-Onion, 5-Sugar Beet, 6-Orchard, 7-Pepper, 8-Rice, 9-Clover).

ID	NDVI Image	Edge Image	Clustered Image	Field Boundaries	Accu-racy (%)
1	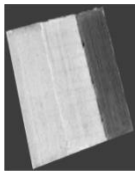	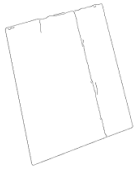	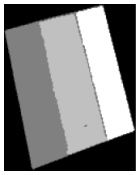	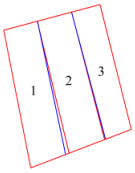	97.99
2	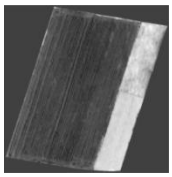			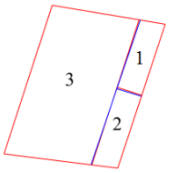	98.71
3	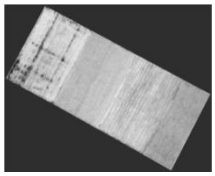	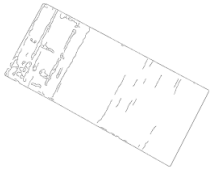	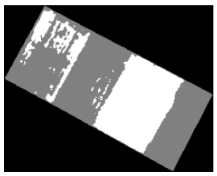	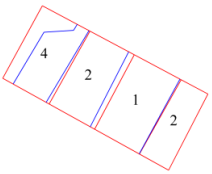	49.85
4	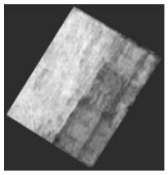	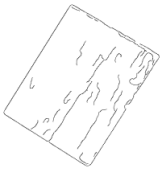		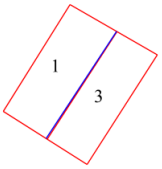	99.07
5	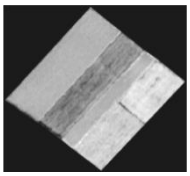	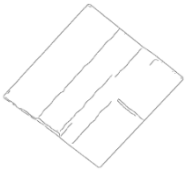	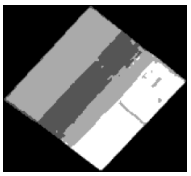	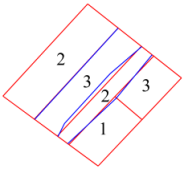	64.98
6	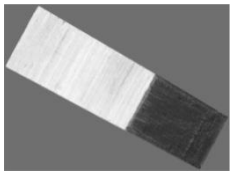	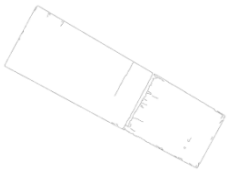	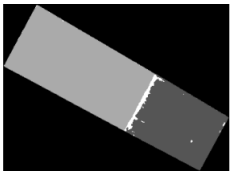	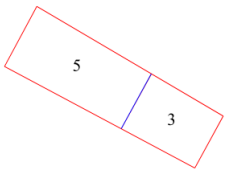	99.90

Table 9. Continued.

ID	NDVI Image	Edge Image	Clustered Image	Field Boundaries	Accu-racy (%)
7	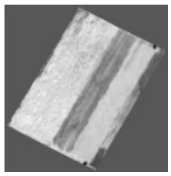	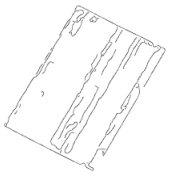		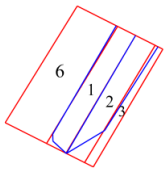	91.05
8	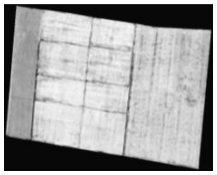	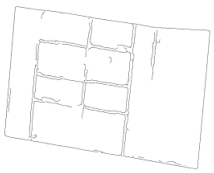	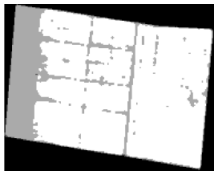	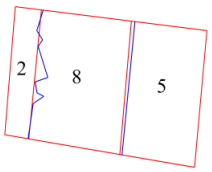	96.37
9	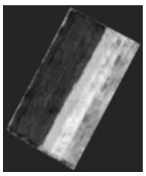	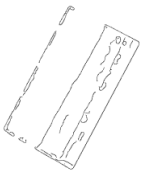	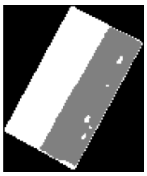	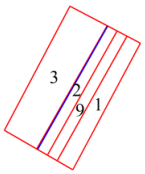	56.15
10	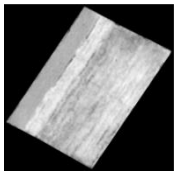	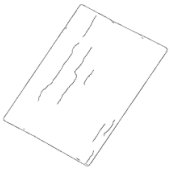	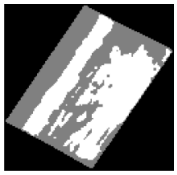	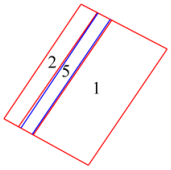	94.63
11	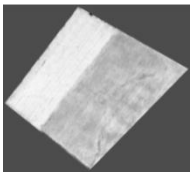	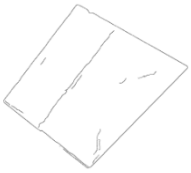	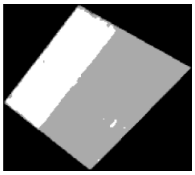	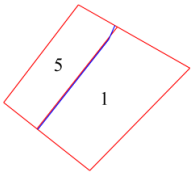	99.05
12	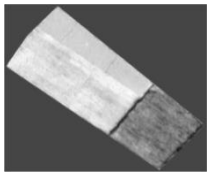	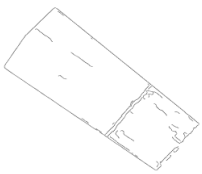	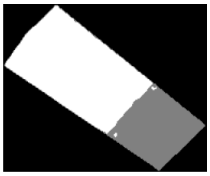	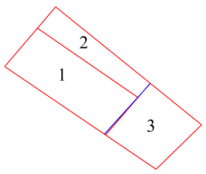	79.41
13	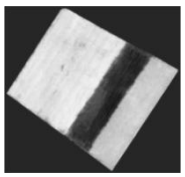		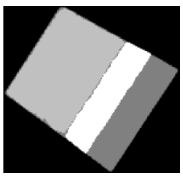	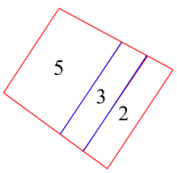	99.47

Table 9. Continued.

ID	NDVI Image	Edge Image	Clustered Image	Field Boundaries	Accu-racy (%)
14	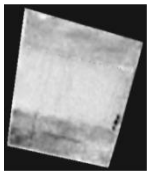	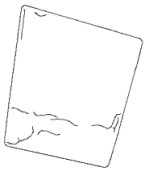		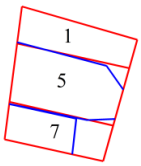	58.44
15	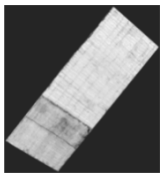	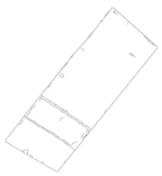	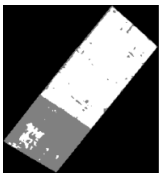	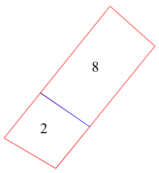	99.86
16	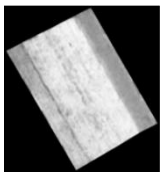	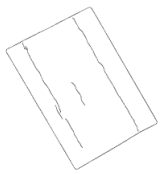	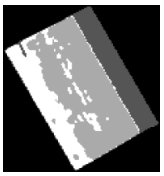	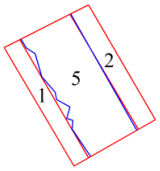	95.79
17	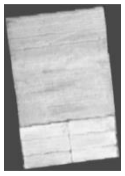			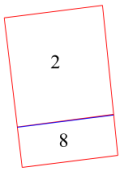	99.56
18	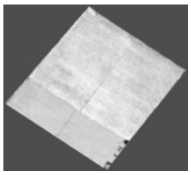	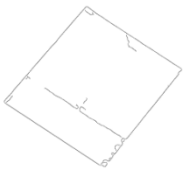	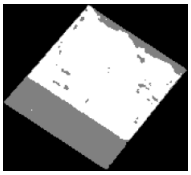	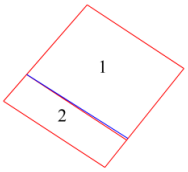	98.92
19				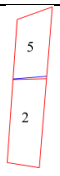	98.97
20					97.33
Overall accuracy					88.78

5. CONCLUSIONS and RECOMMENDATIONS

5.1. CONCLUSIONS

This study proposes an automatic field-based segmentation approach from high resolution satellite images within the permanent boundaries of agricultural fields for the extraction of sub-boundaries between multiple crops (sub-fields) grown within the fields. The segmentation methodology is based on the utilization of both edge detection and automatic FCM clustering. During segmentation, the results of both edge detection and FCM clustering are used to compute external forces for an improved GVF Snake algorithm. The approach starts with edge detection of the image using the Canny edge detector and clustering the image using the automatic FCM clustering algorithm. The external and internal forces are then generated to be used in the improved GVF Snake algorithm. A novel seeding process based on the results of the FCM clustering algorithm is used to initialize the improved GVF Snake algorithm. After completing the evolution of the active contours, the contours near the permanent field boundaries are removed using a boundary masking operation. The final accurate results are obtained after performing a three-stage line simplification operation. An accuracy assessment method based on polygon matching technique is used to evaluate the results.

The proposed within-field segmentation approach was tested on a study area using the Ikonos XS image (with 4 meter spatial resolution), the QuickBird XS image (with 2.44 meter spatial resolution), and the QuickBird PS image (with 0.61 meter spatial resolution). The availability of three different spatial resolution images was an advantage to better evaluate the developed field-based sub-boundary extraction and sub-field construction approach. The results obtained have demonstrated that the proposed approach can be reliably implemented for the extraction of within-field sub-boundaries in agricultural areas. Furthermore, the method provides promising results even the results of either edge detection or automatic FCM clustering are poor. However, if both edge detection and FCM clustering miss to detect a sub-boundary then, the proposed approach may fail to extract that sub-boundary due to inaccurate generation of the external forces which are computed based on the results of edge detection and the clustering. Nonetheless, it is quite evident based on the results achieved in this study that the developed approach is highly robust and provides very high accuracies for the extraction of within-field sub-boundaries from high and very high resolution satellite images. The proposed approach, in which the GVF Snake

algorithm uses the clustered image as the external force, can also be utilized for the extraction of manmade objects, such as buildings and roads through object-based segmentation. The results achieved in this study also illustrate that the GVF Snake algorithm has a good potential in image segmentation when the external forces are calculated accurately to steer the initial contours. However, the GVF Snake algorithm largely depends on the seed points. In this study, this problem has been overcome by means of using the output of the FCM clustering, which is utilized to initialize the algorithm without changing the sensitiveness of the algorithm. It was found that using only the NDVI image as the input for edge detection may in some cases lead to inaccurate results. The results illustrate that the Canny edge detector, the performance of which is known to be superior in general to other operators, appears to provide a good performance for detecting the edges in agricultural fields. However, as it can be known that the results may also very well depend on the input image. In this study, the developed automatic FCM clustering algorithm demonstrated a good performance for finding the correct number of clusters within the permanent field boundaries. Therefore, it can be concluded that the proposed automatic FCM clustering approach was a good choice for the clustering of fields that contain maximum six clusters.

5.2. RECOMMENDATIONS

Based on the results obtained and the observations made in this study, the followings are recommended for the future studies:

1- In this research study, the developed approach was tested on the images of agricultural areas that contain fields with maximum six sub-fields. It is recommended that the efficiency of the approach should be explored by means of performing the tests on areas that contain fields with higher number ofsub-fields.

2- In this study, the GVF Snake algorithm was improved in terms of generating a novel external force and a novel seeding procedure. However, along with the external force the GVF Snake algorithm also uses the internal force in order to evolve the active contours. As a future work, new modifications can be done on the internal forces of the improved GVF Snake algorithm to further increase the reliability of the results.

3- In this study, the results of the automatic FCM clustering were used as the external forces which provided highly satisfactory results by means of overcoming some of the limitations of the traditional GVF Snake algorithm. To further improve the efficiency of the proposed approach other alternative external forces can be used to increase the accuracy of the final outputs.

4- In this research study, a novel post-processing method, which is based on some rational rules and Douglas-Peucker algorithm, was used. For further investigations, it is recommended that other post-processing techniques, such as perceptual grouping method should be used to increase the efficiency of the method.

5- In this study, a novel improved GVF Snake algorithm was used to extract sub-boundaries within agricultural fields. The proposed approach can also be used for the extraction of other natural and manmade objects, such as buildings and roads. Therefore, it is recommended that the developed improved GVF Snake algorithm should be tested for the extraction of different objects to explore its efficiency in different applications.

REFERENCES

[1] WEELS – "Wind Erosion on European Light Soils", *Final report to the European Union Commission. In: Warren, E. (Ed.)*, <http://www2.geog.ucl.ac.uk/weels/report.htm> (accessed 28.10.14), **2014**.

[2] J.E. Anderson, R.L. Fischer and S.R. Deloach, "Remote sensing and precision agriculture: ready for harvest or still maturing?", *Photogrammetric Engineering and Remote Sensing*, vol. 65, no. 10, pp. 1118–1123, **1999**.

[3] X. Blaes, L. Vanhalle, G. Dautrebande, P. Defourny, "Operational control with remote sensing of area-based subsidies in the framework of the common agricultural policy: what role for the SAR sensors?" In: *Proceedings of Third International Symposium on Retrieval of Bio- and Geophysical Parameters from SAR Data for Land Applications*, Sheffield, 11–14 September, pp. 87–92, **2001**.

[4] G. Csornai, I. László, Z. Suba, G. Nádor, E. Bognár, I. Hubik, C. Wirnhardt, G. Zelei, L. Tikász, A. Kocsis, G. Mikus, "The integrated utilization of satellite images in Hungary: operational applications from crop monitoring to ragweed control", In: *Bochenek, Z. (Ed.), New Developments and Challenges in Remote Sensing. Millpress, Rotterdam*, pp. 15–23, **2007**.

[5] E.A. Enclona, P.S. Thenkabail, D. Celis, J. Diekmann, "Within-field wheat yield prediction from IKONOS data: a new matrix approach", *International Journal of Remote Sensing*, vol. 25, no. 2, pp. 377–388, **2004**.

[6] K. Abdul Hakeem, P.V. Raju, "Use of high-resolution satellite data for the structural and agricultural inventory of tank irrigation systems", *International Journal of Remote Sensing*, vol. 30, no. 14, pp. 3613–3623, **2009**.

[7] L.L.F. Janssen, H. Middelkoop, "Knowledge-based crop classification of a Landsat Thematic Mapper image", *International Journal of Remote Sensing*, vol. 13, no. 15, pp. 2827–2837, **1992**.

[8] L.L.F. Janssen, M.N. Jaarsma, E.T.M. Van Der Linden, "Integrating topographic data with remote sensing for land-cover classification", *Photogrammetric Engineering and Remote Sensing*, vol. 56, no. 11, pp. 1503–1506, **1990**.

[9] N.M. Mattikali, B.J. Devereux, K.S. Richards, "Integration of remotely sensed satellite images with a geographical information system", *Computers and Geosciences*, vol. 21, no. 8, pp. 947–956, **1995**.

[10] R.G. Congalton, M. Balogh, C. Bell, K. Green, J.A. Milliken, R. Ottman, "Mapping and monitoring agricultural crops and other land cover in the lower Colorado River Basin", *Photogrammetric Engineering and Remote Sensing*, vol. 64, no. 11, pp. 1107–1113, **1998**.

[11] P. Aplin, P.M. Atkinson, P.J. Curran, "Fine spatial resolution simulated satellite sensor imagery for land cover mapping in the United Kingdom", *Remote Sensing of Environment*, vol. 68, no. 3, pp. 206–216, **1999**.

[12] S. Berberoglu, C.D. Lloyd, P.M. Atkinson, P.J. Curran, "The integration of spectral and textural information using neural networks for land cover mapping in the Mediterranean", *Computers and Geosciences,* vol. 26, no. 4, pp. 385–396, **2000**.

[13] P. Aplin, P.M. Atkinson, "Predicting missing field boundaries to increase perfield classification accuracy", *Photogrammetric Engineering and Remote Sensing*, vol. 70, no. 1, pp. 141–149, **2004**.

[14] M. Turker, M. Arikan, "Sequential masking classification of multi-temporal Landsat7 ETM+ images for field-based crop mapping in Karacabey, Turkey", *International Journal of Remote Sensing*, vol. 26, no. 17, pp. 3813–3830, **2005**.

[15] C. Conrad, S. Fritsch, J. Zeidler, G. Rücker, S. Dech, "Per-field irrigated crop classification in arid Central Asia using SPOT and ASTER data", *Remote Sensing*, vol. 2, no. 4, pp. 1035–1056, **2010**.

[16] M. Turker, A. Ozdarici, "Field-based crop classification using SPOT4, SPOT5, IKONOS and QuickBird imagery for agricultural areas: a comparison study", *International Journal of Remote Sensing,* vol. 32, no. 24, pp. 9735–9768, **2011**.

[17] A. J. W. De Wit and J. G. P. W. Clevers, "Efficiency and Accuracy of Per-Field Classification for Operational Crop Mapping", *International Journal of Remote Sensing*, vol. 25, no. 20, pp. 4091-4112, October **2004**.

[18] M. Turker and E. Derenyi, "GIS assisted change detection using remote sensing", *Geocarto International*, vol. 15, no. 1, pp. 49-54, **2000**.

[19] M. Turker and M. Arikan, "Field-Based Crop Mapping Through Sequential Masking Classification of Multi-Temporal Landsat-7-ETM Images in Karacabey, Turkey", *Conference Paper, ISPRS Istanbul*, **2004**.

[20] M.I. Pedley, P.J. Curran, "Per-field classification: an example using SPOT-HRV imagery", *International Journal of Remote Sensing*, vol. 12, no. 11, pp. 2181–2192, **1991**.

[21] Y. Ban, P.M. Treitz, P.J. Howarth, B. Brisco, R.J. Brown, "Improving the accuracy of Synthetic Aperture Radar analysis for agricultural crop classification", *Canadian Journal of Remote Sensing*, vol. 21, no. 1, pp. 158–164, **1995**.

[22] B. Tso and P. M. Mather, "Crop Discrimination Using Multi-temporal SAR Imagery", *International Journal of Remote Sensing*, vol. 20, no. 12, pp. 2443-

2460, **1999**.

[23] S. Berberoglu, C.D. Lloyd, P.M. Atkinson, P.J. Curran, "The integration of spectral and textural information using neural networks for land cover mapping in the Mediterranean", *Computers and Geosciences*, vol. 26, no. 4, pp. 385–396, **2000**.

[24] G. M. Smith and R. M. Fuller, "An Integrated Approach To Land Cover Classification: an Island of Jersey", *International Journal of Geographical Information Systems,* vol. 22, no. 16, pp. 3123-3142, **2001**.

[25] K. S. Fu, and J. K. Mui, "A survey of image segmentation", *Pattern Recognition,* **1981**.

[26] L. L. F. Janssen and M. Molenaar, "Terrain Objects, Their Dynamics, and Their Monitoring by The Integration of GIS and Remote Sensing", *IEEE Transactions On Geoscience and Remote Sensing*, vol. 33, no. 3, pp. 749- 758, **1995**.

[27] N. R. Pal and S. K. Pal, "A Review on Image Segmentation Techniques", *Pattern Recognition*, **1993**.

[28] C.Y. Ji, "Delineating agricultural field boundaries from TM imagery using dyadic wavelet transforms", *ISPRS Journal of Photogrammetry and Remote Sensing*, vol. 51, no. 6, pp. 268–283, **1996**.

[29] A. Rydeberg and G. Borgefors, "Integrated Method for Boundary Delineation of Agriculture Fields In Multispectral Satellite Images", *IEEE Transactions on Geoscience and Remote Sensing*, vol. 39, no. 11, pp. 2514-2520, **2002**.

[30] M. Mueller, K. Segl, H. Kaufmann, "Edge- and region-based segmentation technique for the extraction of large, man-made objects in high-resolution satellite imagery", *Pattern Recognition,* vol. 37, no. 8, pp. 1619–1628, **2004**.

[31] T. Ishida, S. Itagaki, Y. Sasaki, H. Ando, "Application of wavelet transform for extracting edges of paddy fields from remotely sensed images", *International Journal of Remote Sensing,* vol. 25, no. 2, pp. 347–357, **2004**.

[32] M. Turker, E.H. Kok, "Automatic extraction of sub-boundaries within agricultural fields from remote sensing images", In: *2nd Workshop of the EARSeL Special Interest Group on Land Use and Land Cover, Bonn,* (on CDROM), 28–30 September **2006**.

[33] M., Turker, E. H. Kok, "Field-based sub-boundary extraction from remote sensing imagery using perceptual grouping", *ISPRS journal of photogrammetry and*

remote sensing , vol. 79, pp. 106-121, **2013**.

[34] M. Kass, A. Witkin, D. Terzopoulos, "Snakes: active contour models", *International Journal of Computer Vision*, vol. 1, no. 4, pp. 321–331, **1988**.

[35] M. Torre, P. Radeva, "Agricultural field extraction from aerial images using a region competition algorithm", *International Archives of Photogrammetry and Remote Sensing*, XXXIII (Part B3), pp. 889–896, **2000**.

[36] M. Butenuth, B.M. Straub, C. Heipke, "Automatic extraction of field boundaries from aerial imagery", In: *KDNet Symposium: Knowledge Based Services for the Public Sector, Bonn*, 3–4 June, p. 12, **2004**.

[37] P.S. Tiwari, H. Pande, M. Kumar, V.K. Dadhwal, "Potential of IRS P-6 LISS IV for agriculture field boundary delineation", *Journal of Applied Remote Sensing*, vol. 3, pp. 1–9, **2009**.

[38] M. Butenuth, C. Heipke, "Network snakes: graph-based object delineation with active contour models", *Machine Vision and Applications*, vol. 23, no. 1, pp. 91-109, **2012**.

[39] J. Canny, "A Computational Approach to Edge Detection", *IEEE Transactions on Pattern Analysis and Machine Intelligence*, **1986**.

[40] Wen-Jan Chen, Chin-Chen Chang, T. Hoang Ngan Le, "High payload steganography mechanism using hybrid edge detector" Expert Systems with Applications 37 (2010) 3292–3301 , 2009 Elsevier Ltd..

[41] L. A. Zadeh, "Fuzzy sets", *Information Control*, vol. 8, pp. 338-353, **1965**.

[42] L. A. Zadeh, "Fuzzy sets a basic for atheory of possibility", *Fuzzy Sets Systems*, vol. 1, pp. 3-28, **1978**.

[43] J. C. Bezdek, "Pattern Recognition With Fuzzy Objective Function Algorithm", Plenum, New York, **1981**.

[44] C. Xu, J. L. Prince, "Gradient vector felow: A new external force for snakes*", in Proceedings of Conference on Computer Vision and Pattern Recognition*, pp. 66-71, **1997**.

[45] J. Hershberger and J. Snoeyink, "Speeding Up the Douglas-Peucker Line-Simplification Algorithm", *Technical Report, In Proceedings of 5th International Symposium of Spatial Data Handling*, pp. 134-143, **1992**.

[46] N.R. Chrisman, "Modeling error overlaid categorical maps", *In: Goodchild, M.F., Gopal, S. (Eds.), Accuracy of Spatial Databases. Taylor and Francis, London*, pp. 21–34, **1989**.

[47] Gong P., Marceau D., and Howarth P. J., "A comparison of spatial feature extraction algorithms for land-use mapping with SPOT HRV data", *Remote Sensing of Environment,* Vol. 40, pp. 137-151, **1992**.

[48] Gong P. and Howarth P. J., "Frequency-based contextual classification and grey-level vector reduction for land-use identification", *Photogrammetric Engineering and Remote Sensing,* Vol. 58, pp. 423-437, **1992**.

[49] Cheng Y., "Mean shift, mode seeking, and clustering", *IEEE Transactions on Pattern Analysis and Machine Intelligence,* Vol. 17, pp. 790-799, **1995**.

[50] Rosenfeld A. and Thurston M., "Edge and curve detection for visual scene analysis", *IEEE Transactions on Computers,* Vol. 20, pp. 562-569, **1971**.

[51] Nakayama K. and Shimojo S., "Experiencing and perceiving visual surfaces", *Science,* Vol. 257, pp. 1357-1363, **1992**.

APPENDIX

A. The small portion of the developed MATLAB Codes for the proposed method.

```
%input data:
% k      - Image (including 4 band), this code is particularly for
% Ikonos images due to some parameters adapted for ikonos images.
% thresh - Threshold for Fuzzy c-means clustering step
% x5, y5 - are coordinates for the original field boundaries.
% refx, refy - are coordinates for the reference lines, which are used in
% accuracy assessment step


   k=imread('ikonos15.tif');
   thresh=0.8;

   % primary boundaries of the permanent fields

  x5=[3 95 134 47 3];y5=[117 3 37.5 144 117];% primary boundaries
  refx=[3 34.23 76.79 47 3; 34.23 95 134 76.79 34.23];refy=[117 78.3
107.5 144 117;78.3 3 37.5 107.5 78.3];% References

   % get image and split image to its bands individually
   image=k;
   rgb(:,:,1)=double(image(:,:,1));
   rgb(:,:,2)=double(image(:,:,2));
   rgb(:,:,3)=double(image(:,:,3));

   % Transform format of the images(splitted band images) to double
format
   % in order to have more accurate calculation process
   rgb_r=double(image(:,:,1));
   rgb_g=double(image(:,:,2));
   rgb_b=double(image(:,:,3));
   nir=double(image(:,:,4));

  % compute the ndvi image from RED and NIR bands of the image
   ndvi=((nir-rgb_r)./(nir+rgb_r));
   % imshow(ndvi,[]);

   % increase the size of the whole image for 2 pixels from each side in
   % order to block active contours from proceeding to out of the image
   j1=ndvi;
      mm=0;
   j=imresize(j1,1);
   [s1 s2]=size(j);
   ss1=s1+4;ss2=s2+4;
    jj=zeros(ss1,ss2);
   for nsj1=1:s1
       for nsj2=1:s2
  jj((nsj1+2),(nsj2+2))=j(nsj1,nsj2);
       end
   end

   % apply median filter to reduce the noises in the image
   z1 = medfilt2(jj,[7 7]);
```

```
    ko=isnan(jj);
   for ff1=1:ss1
       for ff2=1:ss2
            if ko(ff1,ff2)==1
              jj(ff1,ff2)=0;
            end

       end
   end
```

.
.
.
.
.
.

```
% find the intersection points between contours to extend contours to
    % reach original major fields' boundaries
     dp(1,:)=y3;
     dp(2,:)=x3;

      xy=intersectpoint118nv6(dp(2,:),dp(1,:),x5,y5,jj);
      x3=xy(1,:);
      y3=xy(2,:);
     y3(isnan(y3))=[];
     x3(isnan(x3))=[];

     dp2=[];

      dp2(1,:)=x3;
     dp2(2,:)=y3;

  % line simplification operation (Dougles-Peucker algorithm)
     dp1=simplifyPoly(2,dp2);

     y4=dp1(2,:);
     x4=dp1(1,:);

 % display the final segment result for each sub-field boundary which is
derived out from each cluster
      dp=[];
      hold off
      x2{r,d}=double(x4);
      y2{r,d}=double(y4);

    end
end
end

% after running the algorithm for each cluster (sub-field) and gathering
the
% results (segments' coordinates) in one variable, the algorithm start to
% form the polygons to find out appropriate connections among points
[xf yf]=formpoly15(x2,y2,x5,y5,jj);

close all;
```

```
% finalizing the forming polygon operation and accuracy assessment
algorithm
[ov mac]=end14(xf,yf,x5,y5,refx,refy,jj);

%Show the segmentation results
subplot(221); imshow(jj,[]); title('Test Image');
subplot(222); imshow(pixel_labels,[ ]), title('Cluster Image');
subplot(223); imshow(s), title('Edge Image');
```

CURRICULUM VITAE

Credentials

Name, Surname	:	Saman GHAFFARIAN
Place of Birth	:	Tabriz, Iran
Marital Status	:	Single
E-mail	:	ghaffarian.saman@gmail.com
Address	:	Geomatics Engineering Department of Hacettepe University Beytepe - ANKARA

Education

High School	:	Medeni High School, Iran
BSc.	:	Civil Engineering, Islamic Azad University, Iran
MSc.	:	-
PhD.	:	-

Foreign Languages

English, Persian

Work Experiences

-

Areas of Experiences

-

Projects and Budgets

-

Publications

-

Oral and Poster Presentations

-